Journal of Computational Physics (2018)

Contents lists available at ScienceDirect

Journal of Computational Physics

journal homepage: www.elsevier.com/locate/jcp

Time-accurate calculation of two-phase granular flows exhibiting compaction, dilatancy and nonlinear rheology

Davide Monsorno[a], Athanassios A. Dimas[b], Miltiadis V. Papalexandris[a,*]

[a] *Institute of Mechanics, Materials and Civil Engineering, Université catholique de Louvain, 1348 Louvain-la-Neuve, Belgium*
[b] *Departement of Civil Engineering, University of Patras, 26500 Patras, Greece*

ARTICLE INFO

Article history:
Received DRAFT

Keywords: granular suspensions, two-phase flows, sedimentation, material interfaces, projection method

ABSTRACT

In this paper we propose a time-accurate algorithm for the calculation of two-phase granular flows via two-velocity, two-pressure Eulerian models. Such flows exhibit a number of important characteristics that make their computation particularly challenging. For example, even at constant-density flows the suspended granular phase can compact or expand so that the velocity fields of the two phases are not solenoidal. Also, the granular material typically exhibits a complex and highly nonlinear rheological behaviour. Moreover, the governing equation for the granular volume fraction (often referred to in the literature as "compaction equation" or "particle migration model") involves stresses as source terms and, therefore it is strongly coupled to the momentum balance laws. Herein we show that this coupling can be a strong destabilising factor in the computations if it is not treated properly. Our algorithm is based on a predictor-corrector time-integration scheme. Further, it employs a generalized double projection method for non-solenoidal velocity fields that results in second-order elliptic equations for the phasial pressures. The efficiency of the proposed algorithm is illustrated via a series of simulations of transient flows with strong concentration gradients, namely, sedimentation of a granular suspension, compaction of a dense sediment bed, and collapse of a submerged granular column. Numerical grid-convergence studies further show that the algorithm exhibits satisfactory convergence rates. Overall, these numerical results indicate that the proposed algorithm is well suited for the simulation of flows of dense suspensions, flows with high volume-fraction variations or material interfaces, as well as for unsteady fluid-solid interaction problems.

*Corresponding author
e-mail: miltos@uclouvain.be (Miltiadis V. Papalexandris)

1. Introduction

Granular materials, defined as conglomerates of solid particles, are encountered in numerous natural phenomena and technological applications. Actually, the industrial processing of grains represents approximately 10% of the global energy consumption [1], and granular aggregates are the second most manipulated class of materials behind water [2]. They are typically characterized by dissipative interactions between grains and present an extremely rich and unexpected phenomenology even when the physics of particle interactions at the grain level is well understood. For example, granular materials can flow, support shear stress at equilibrium, compact, dilatate, clog and segregate. In fact, their macroscopic behaviour can be so different from what is common for fluids or solids, that it has been proposed to consider them as an independent state of matter [3].

In problems of practical interest, granular materials are saturated by a carrier fluid, such as air or water, the presence of which can rarely be neglected. This is so because a carrier fluid increases the mobility of the grains which causes significant momentum exchange between the two phases, often involving quite complex physical mechanisms. This holds true at both high and low density ratios between the two phases. As pointed out in [4], even in the case of dry compacted grains one must account for the presence of air. Further, in the case of a liquid carrier such as water, in addition to causing interphasial momentum exchange, the liquid also mediates the interactions between solid particles.

When the particles are large enough that Brownian motion can be neglected, which is generally the case for particles above the micrometer scale [5], fluid-solid particle mixtures are referred to as *granular suspensions*. The behaviour of granular suspensions differs sharply from the one of simple fluids. For example, even smooth rigid spheres are known to exhibit non-Newtonian rheological behaviour when suspended in a liquid [6]. An Eulerian continuum modelling of granular suspensions is desirable in practical applications, since flows of interest involve very large numbers of particles. Thus far, several descriptions of the rheology of granular suspensions have been put forward. Some of them have been derived on the basis of experimental data and scaling arguments for steady shear flows [7–9], while some others have been derived within the framework of a continuum-mechanics approach [10–12]; see the review article [13] for additional references.

However, despite these advancements, the development of algorithms and simulation techniques that can treat unsteady and multidimensional granular flows is still at an early stage. The design of general-purpose algorithms for granular suspensions involves several computational issues. Some of them arise from the coexistence of the two phases in space. For example, even at constant-density flows the suspended granular phase can compact or expand so that the velocity fields of the two phases are not solenoidal. As a result, the extension of popular techniques developed for incompressible single-phase flows is not straightforward. Also, since the phasial velocities have a non-zero divergence, both phases are subject to bulk viscous stresses that must be accounted for.

Additional computational issues arise from the complexity of the constitutive laws for the granular rheology. These are highly nonlinear functions of the strain rate and, moreover, involve viscosity coefficients that are stiff with respect to variations of the granular volume fraction. Also, granular flows can exhibit sharp transitions between dense and dilute regions of the flow and very steep gradients of particle concentration which require the introduction of interface-regularization schemes. Further, the rate equation for the granular volume fraction, often referred to as "compaction equation" or "particle-migration model", involves stresses as source terms, whereas the stresses in the momentum equations appear inside divergence terms (fluxes). For this reason, the integration of this equation is far from trivial and requires particular attention. Due to these difficulties, the currently available algorithms cannot accomodate large variations in particle concentration and they are further limited to simple flow geometries and rudimentary rheological models [14–19]. Consequently, numerical results can be found only for special cases, such as steady-state or quasi-1D flows, or flows that can be approximated as solenoidal.

In this paper we present a numerical algorithm for unsteady granular flows that exhibit compaction, dilatancy and non-Newtonian rheological behaviour. We also apply this algorithm to the governing equations for granular suspensions derived in [12] and present numerical results for unsteady flows with sedimentation and steep volume-fraction gradients; these are typical examples of processes in which the divergence of the phasial velocities cannot be neglected. The proposed algorithm is based on a predictor-corrector scheme for the time-integration of the governing equations. It employs a generalised projection method for the computation of the phasial pressures. This amounts to taking the divergence of the momentum balance law of each phase separately and combining it with the corresponding mass-balance laws and volume-fraction equation so as to obtain a second-order elliptic PDE for the pressure of each phase.

The proposed algorithm has been formulated with respect to the flow model [12] but it is applicable to a wide class of two-velocity two-pressure models for fluid-solid mixtures by virtue of the similarities in their structure. In

the context of granular suspensions, these are known as *suspension-balance models* [20] and may involve different types of compaction equation all of which can be treated with the numerical procedures described herein. To our knowledge, this is the first projection method for multiphase flow models that contain stresses as source terms and that involve a strong coupling between the momentum balance laws and the compaction equation. Another novel feature is that the proposed algorithm can simultaneously handle highly complex rheology laws and stiff physical parameters that diverge at the point of maximum packing. Moreover, it can accommodate large variations of the particle concentration, i.e. it can handle both dilute and dense suspensions.

The paper is organized as follows. In Section 2 we present the governing equations and discuss the critical issues concerning their numerical treatment. In Section 3 we describe the proposed numerical algorithm. In Section 4 we present numerical results for unsteady processes, such as the sedimentation of a suspension in a tube and the collapse of a submerged granular column. These simulations serve as validation tests and illustrate the efficiency of our algorithm. Finally, Section 5 concludes.

2. Governing equations

Let us consider a mixture of an isotropic granular material and a Newtonian fluid. We assume that both phases have constant density. The volume fractions of the fluid and granular phases are denoted by ϕ_f and ϕ_s, respectively. The mixture is assumed to be saturated, so that the following saturation relation holds,

$$\phi_f + \phi_s \;=\; 1\,. \tag{1}$$

Further, each phase is endowed with its own mass and momentum balance laws. In dimensionless form, these laws read as follows.
Fluid phase

$$\frac{\partial \phi_f}{\partial t} + \nabla\cdot(\phi_f \boldsymbol{u}_f) \;=\; 0\,, \tag{2}$$

$$\rho_f \frac{\partial \phi_f \boldsymbol{u}_f}{\partial t} + \rho_f \nabla\cdot(\phi_f \boldsymbol{u}_f \otimes \boldsymbol{u}_f) \;=\; \nabla\cdot\boldsymbol{\Pi}_f - \boldsymbol{f} + \rho_f \phi_f \boldsymbol{g}\,. \tag{3}$$

Granular phase

$$\frac{\partial \phi_s}{\partial t} + \nabla\cdot(\phi_s \boldsymbol{u}_s) \;=\; 0\,, \tag{4}$$

$$\rho_s \frac{\partial \phi_s \boldsymbol{u}_s}{\partial t} + \rho_s \nabla\cdot(\phi_s \boldsymbol{u}_s \otimes \boldsymbol{u}_s) \;=\; \nabla\cdot\boldsymbol{\Pi}_s + \boldsymbol{f} + \rho_s \phi_s \boldsymbol{g}\,. \tag{5}$$

In the above equations,the subscripts "f" and "s" denote quantities relative to the fluid and granular phase, respectively, while the symbol $\otimes$ stands for the dyadic product between two vectors. Also, ρ_α and $\boldsymbol{u}_\alpha = (u_{\alpha_x}, u_{\alpha_y}, u_{\alpha_z})$, $\alpha = f, s$, stand for the density and velocity vector of the phase α, while $\boldsymbol{g}$ denotes the gravitational acceleration. Further, the quantity $\boldsymbol{f}$ represents momentum exchange between the two phases, while $\boldsymbol{\Pi}_f$ and $\boldsymbol{\Pi}_s$ represent the stress tensors of the fluid and granular phase, respectively.

The above system is closed with constitutive relations for $\boldsymbol{f}$, $\boldsymbol{\Pi}_f$ and $\boldsymbol{\Pi}_s$, and with an evolution equation for ϕ_s. According to the thermo-mechanical theory of Monsorno et al. [12], the interphasial momentum exchange $\boldsymbol{f}$ is given as the sum of a drag term and a nozzling term,

$$\boldsymbol{f} \;=\; \delta\,(\boldsymbol{u}_f - \boldsymbol{u}_s) + p_f \nabla\phi_s\,, \tag{6}$$

where p_f is the static pressure of the fluid phase and δ the interphasial drag coefficient.

The stresses acting on the fluid phase are the static pressure p_f and the viscous stresses, i.e.

$$\boldsymbol{\Pi}_f \;=\; -\phi_f p_f \mathbf{I} + \frac{1}{\mathrm{Re}}\mathbf{T}_f\,, \tag{7}$$

where Re is the Reynolds number, $\mathbf{I}$ is the identity matrix and $\mathbf{T}_f$ is the viscous-stress tensor. As mentioned above, the fluid phase is Newtonian and, therefore, its viscous-stress tensor is given by

$$\mathbf{T}_f \;=\; \phi_f \zeta_f\,(\nabla\cdot\boldsymbol{u}_f)\,\mathbf{I} + 2\phi_f \mu_f \mathbf{V}_f^{\mathrm{d}}\,, \tag{8}$$

with μ_f and ζ_f being the fluid's shear and bulk viscosities, respectively. Also, $\mathbf{V}_f$ stands for the strain-rate tensor of the fluid phase and and $\mathbf{V}_f^{\mathrm{d}}$ represents the deviatoric part of $\mathbf{V}_f$, i.e. $\mathbf{V}_f^{\mathrm{d}} = \mathbf{V}_f - \frac{2}{3}(\nabla\cdot\boldsymbol{u}_f)\mathbf{I}$.

The stresses acting on the granular phase are the static pressure p_s, additional elastic stress due to the microstructure of the system $\mathbf{C}_s$ and the viscous stresses $\mathbf{T}_s$. In other words, we have that

$$\boldsymbol{\Pi}_s \;=\; -\phi_s p_s\,\mathbf{I} + \mathbf{C}_s + \frac{1}{\mathrm{Re}}\mathbf{T}_s\,. \tag{9}$$

According to [21, 22], the tensor $\mathbf{C}_s$ is given by

$$\mathbf{C}_s \;=\; \gamma_s \nabla\phi_s \otimes \nabla\phi_s\,, \tag{10}$$

and describes Korteweg-type stresses due to variations in the density of the contact area between grains. In the literature, this term is sometimes referred to as "configuration stress tensor" since it depends on the distribution of grains in space. Also, its components are referred to as "nonlocal stresses" because they depend on the grain size. These stresses are elastic, i.e. they produce reversible work, and as such they are present at equilibrium. The quantity γ_s that appears in (10) is defined as the derivative of the Helmholtz free energy of the granular phase with respect to $\nabla\phi_s$; see relevant discussions in [21–24].

The granular phase is characterized by non-Newtonian rheology, i.e. the granular viscous stresses are nonlinear with respect to the deformation tensor. Monsorno et al. [12] proposed the following constitutive law for these stresses,

$$\mathbf{T}_s \;=\; \left((\zeta_{s1}+\zeta_{s2})\,\nabla\cdot\boldsymbol{u}_s + \chi_1\right)\phi_s\,\mathbf{I} + 2(\mu_{s1}+\mu_{s2})\phi_s\mathbf{V}_s^{\mathrm{d}} \;+\chi_2\phi_s\mathbf{V}_s\cdot\mathbf{V}_s\,. \tag{11}$$

In this relation, the coefficients μ_{s1} and ζ_{s1} are independent of the strain rate and are equivalent to the shear and bulk viscosity in simple fluids. On the other hand, the quantities μ_{s2}, ζ_{s2}, χ_1 and χ_2 do depend on the strain rate and are given by

$$\mu_{s2} \;=\; \frac{\mu_{\mathrm{n}}}{\sqrt{2}}\frac{\det\mathbf{V}_s}{(\mathbf{V}_s{:}\mathbf{V}_s)^{\frac{3}{2}}}\,, \qquad \zeta_{s2} \;=\; \frac{\mu_{\mathrm{n}}\sqrt{2}}{3}\frac{\det\mathbf{V}_s}{(\mathbf{V}_s{:}\mathbf{V}_s)^{\frac{3}{2}}} \tag{12}$$

and

$$\chi_1 \;=\; -\sqrt{2}\,\mu_{\mathrm{n}}\left(2\sqrt{\mathbf{V}_s^{\mathrm{d}}{:}\mathbf{V}_s^{\mathrm{d}}} - \frac{3}{2}\frac{\mathbf{V}_s^{\mathrm{d}}{:}\mathbf{V}_s^{\mathrm{d}}}{\sqrt{\mathbf{V}_s{:}\mathbf{V}_s}}\right), \qquad \chi_2 \;=\; -\frac{\sqrt{2}\,\mu_{\mathrm{n}}}{\sqrt{\mathbf{V}_s{:}\mathbf{V}_s}}\,. \tag{13}$$

In these expressions, the symbol : stands for the double interior product between two tensors. Further, μ_{n} is the so-called "normal viscosity" [8] and is also independent of the strain rate. Thus, the granular rheology is characterised by three independent viscosity coefficients. Moreover, $\mathbf{V}_s$ and $\mathbf{V}_s^{\mathrm{d}}$ stand for the strain-rate tensor of the granular phase and its deviatoric component, respectively, $\mathbf{V}_s^{\mathrm{d}} = \mathbf{V}_s - \frac{2}{3}(\nabla\cdot\boldsymbol{u}_s)\mathbf{I}$.

According to [12], the volume fraction ϕ_s satisfies the following *compaction equation*,

$$\frac{\partial\phi_s}{\partial t} + \boldsymbol{u}_s\cdot\nabla\phi_s = \mathrm{Re}\,\frac{\phi_s\phi_f}{\mu_c}\left(p_s - p_f - \beta_s + \nabla\cdot(\gamma_s\nabla\phi_s)\right). \tag{14}$$

This equation plays the role of the particle-migration model for the granular phase. The quantity μ_c is a transport coefficient that measures dissipative relaxation due to compaction of the granular phase. It has dimensions of viscosity and for this reason it is referred to as "compaction viscosity" [25]. The term β_s stands for the intergranular stress, sometimes referred to as "configuration pressure", and describes the resistance of the granular material to compaction. Formally, it is defined as the derivative of the Helmholtz free energy of the granular material with respect to ϕ_s; see, for example, [12] and the relevant discussions in [21, 22, 24, 26–28].

Finally, we remark that the governing system (2) – (14) and all the above constitutive relations are made dimensionless with respect to a reference state of the fluid phase. Accordingly, the Reynolds number Re is defined with respect to the (dimensional) fluid density and shear viscosity. On the other hand, the dimensionless values of these two variables are $\rho_f = 1$ and $\mu_f = 1$, respectively.

3. Description of the numerical method

The proposed algorithm can be classified as a generalised projection method for multi-phase flows. The original projection method was introduced by Chorin [29] and independently by Temam [30] for the constant-density Navier-Stokes equations. Its main concept is to combine the divergence of the momentum equation with the continuity equation, according to which the velocity field is divergence-free when the density is constant, so as to derive an elliptic equation for the pressure. Over the years, the projection method has been successfully extended to a variety of cases with divergent velocity fields, such as single-phase variable-density flows [31, 32], porous-media flows [33, 34], and flows with solid particles [17, 35].

3.1. Major computational challenges

In the extension of the Chorin-Temam projection method to variable-density flows, the most crucial step is to provide a stable discretization for the time derivative of the density that enters the elliptic equation for the pressure via the continuity equation. The presence of this derivative is known to have a destabilizing effect in the numerical solution of the elliptic equation [36]. The same situation arises in two-phase flows at constant density for the time derivative of the volume fraction, cf. equations (2) and (4). Moreover, with regard to the numerical treatment of the above governing system of equations, one is confronted with major additional challenges. These are the following.

Size and complexity. The governing system consists of three scalar and two vectorial partial differential equations. Further, these equations are highly nonlinear and coupled with each other.

Presence of non-conservative products. The non-conservative product $p_f \nabla \phi_s$ of (6) describes interphasial momentum exchange and enters the momentum equations (3) and (5). This has important consequences in the computation of the phasial pressures p_s and p_f. For example, whereas the classical Chorin-Temam projection method for the Navier-Stokes equations yields a Poisson equation for the pressure, generalizations of this method to the system in hand (2)– (5) result in elliptic equations that are more challenging to discretize and solve numerically.

Stiff material parameters. In accordance with experimental observations, the available correlations for the intergranular stress β_s and the viscosity coefficient μ_s are stiff nonlinear functions of the volume fraction ϕ_s and become singular at maximum packing, i.e. at the point of jamming transition.

Divergent velocity fields. From the continuity equations (2) and (4) and the compaction equation (14), it can be seen that the velocity fields $\boldsymbol{u}_s$ and $\boldsymbol{u}_f$ are not solenoidal, even at constant densities. In particular, the divergence of $\boldsymbol{u}_s$ can be given in terms of the following expression,

$$\nabla \cdot \boldsymbol{u}_s = -\mathrm{Re}\frac{\phi_f}{\mu_c}\left(p_s - \beta_s - p_f + \nabla \cdot (\gamma_s \nabla \phi_s)\right). \tag{15}$$

On the basis of the compaction equation (14), we readily deduce that the left-hand side of (15) vanishes only when the mixture is at rest. This complicates even further the application of projection methods for the calculation of the phasial pressures.

Normal stresses appear as source terms. The pressures p_s and p_f appear explicitly as source terms in the compaction equation (14). This renders the computation of the volume fraction quite sensitive with respect to the magnitude of these quantities and the magnitude of their difference. By contrast, the Navier-Stokes equations involve only the gradient of the pressure.

Nonlinear rheology. The granular viscous stresses are given in terms of the rate-dependent and nonlinear constitutive relations (11), (12) and (13). These stresses play an important role to the evolution of the granular phase, especially in the cases of dense suspensions and granular beds.

All of these issues are addressed in the present work.

3.2. Time discretization

For computational purposes it is convenient to introduce the auxiliary pressures p_d and p'_f,

$$p_d = (p_s - p_f)\phi_s, \qquad p'_f = p_f - \rho_f \Phi, \quad \text{with} \quad \Phi = \int \boldsymbol{g} \cdot \mathrm{d}\boldsymbol{x}. \tag{16}$$

In the above expression the integration constant for the potential Φ is inconsequential, as only the gradient of p'_f enters the governing equations. By employing these definitions and by inserting the constitutive relations (6), (7) and (9) in the mass and momentum balance laws (2) – (5), the two-phase flow model in hand can be cast in the following form,

$$\frac{\partial \phi_f}{\partial t} + \nabla\cdot(\phi_f \boldsymbol{u}_f) \;= 0\,, \tag{17}$$

$$\rho_f \frac{\partial \phi_f \boldsymbol{u}_f}{\partial t} + \rho_f \nabla\cdot(\phi_f \boldsymbol{u}_f \otimes \boldsymbol{u}_f) + \phi_f \nabla p'_f \;= \frac{1}{\mathrm{Re}}\nabla\cdot\mathbf{T}_f \; - \delta(\boldsymbol{u}_f - \boldsymbol{u}_s)\,, \tag{18}$$

$$\frac{\partial \phi_s}{\partial t} + \nabla\cdot(\phi_s \boldsymbol{u}_s) \;= 0\,, \tag{19}$$

$$\rho_s \frac{\partial \phi_s \boldsymbol{u}_s}{\partial t} + \rho_s \nabla\cdot(\phi_s \boldsymbol{u}_s \otimes \boldsymbol{u}_s) + \nabla p_d \;= \frac{1}{\mathrm{Re}}\nabla\cdot\mathbf{T}_s - \nabla\cdot\mathbf{C}_s + \delta(\boldsymbol{u}_f - \boldsymbol{u}_s) - \phi_s \nabla p'_f + (\rho_s - \rho_f)\phi_s \boldsymbol{g}\,, \tag{20}$$

$$\frac{\partial \phi_s}{\partial t} + \boldsymbol{u}_s\cdot\nabla\phi_s \;= \mathrm{Re}\,\frac{\phi_s \phi_f}{\mu_c}\left(\frac{p_d}{\phi_s} - \beta_s + \nabla\cdot(\gamma_s \nabla\phi_s)\right), \tag{21}$$

where $\phi_f = 1 - \phi_s$. The unknown variables in this system are $\boldsymbol{u}_f$, $\boldsymbol{u}_s$, p'_f, p_d and ϕ_s, We observe that only the gradients of p_d and p'_f appear in the momentum equations (18) and (20). Additionally, gravity enters explicitly (20) but does not appear in (18).

The algorithm presented herein is a predictor-corrector, fractional-step method that employs a second-order semi-implicit time-marching scheme. In what follows, the time step is assumed to be Δt. The superscripts n, $*$ and $n+1$ designate the computed values at time $n\Delta t$, the predicted values and the corrected values at $(n+1)\Delta t$, respectively.

3.2.1. Predictor stage

1) The predicted value of the volume fraction ϕ_s^* is computed from the compaction equation (21) via the following scheme,

$$\frac{\phi_s^* - \phi_s^n}{\Delta t} \;= \mathrm{Re}\frac{\phi_s^n \phi_f^n}{\mu_c}\nabla\cdot\left(\frac{\gamma_s^n}{2}\left(\nabla\phi_s^* + \nabla\phi_s^n\right)\right) + \mathrm{Res}_\phi^*\,, \tag{22}$$

where the residual Res_ϕ is defined as follows,

$$\mathrm{Res}_\phi \;= -\boldsymbol{u}_s\cdot\nabla\phi_s + \mathrm{Re}\,\frac{\phi_f}{\mu_c}\left(p_d - \phi_s\beta_s\right)\,. \tag{23}$$

Following [37], the term Res_ϕ^* in equation (22), is approximated by a second-order Adams-Bashforth method, i.e.

$$\mathrm{Res}_\phi^* \;= \frac{3\mathrm{Res}_\phi^n - \mathrm{Res}_\phi^{n-1}}{2}\,. \tag{24}$$

2) Next, the momentum equation of the granular phase (20) is discretized as follows,

$$\begin{aligned}\frac{\phi_s^* \boldsymbol{u}_s^* - \phi_s^n \boldsymbol{u}_s^n}{\Delta t} + \frac{1}{\rho_s}\nabla p_d^* \;= {}& \frac{1}{\rho_s \mathrm{Re}}\nabla\cdot\left(\left(\mu_{s1}\phi_s \mathbf{V}_s^{\mathrm{d}}\right)^* + \left(\mu_{s1}\phi_s \mathbf{V}_s^{\mathrm{d}}\right)^n\right) \\ & \frac{1}{2\rho_s \mathrm{Re}}\nabla\cdot\left(\left(\zeta_{s1}\phi_s \nabla\cdot\boldsymbol{u}_s\right)^* \mathbf{I} + \left(\zeta_{s1}\phi_s \nabla\cdot\boldsymbol{u}_s\right)^n \mathbf{I}\right) + \\ & \mathbf{Res}_s^* + \frac{\rho_s - \rho_f}{\rho_s}\phi_s^* \boldsymbol{g}\,,\end{aligned} \tag{25}$$

where the residual $\mathbf{Res}_s$ is given by

$$\begin{aligned}\mathbf{Res}_s \;= {}& -\nabla\cdot(\phi_s \mathbf{u}_s \otimes \mathbf{u}_s) + \nabla\cdot\left(\frac{\gamma_s}{\rho_s}\nabla\phi_s \otimes \nabla\phi_s\right) - \phi_s \nabla\left(\frac{p'_f}{\rho_s}\right) + \frac{\delta}{\rho_s}\left(\boldsymbol{u}_f - \boldsymbol{u}_s\right) \\ & + \frac{1}{\rho_s \mathrm{Re}}\nabla\cdot\left(\left(\zeta_{s2}\nabla\cdot\boldsymbol{u}_s + \chi_1\right)\phi_s \mathbf{I} + 2\mu_{s2}\phi_s \mathbf{V}_s^{\mathrm{d}} + \chi_2 \phi_s \mathbf{V}_s\cdot\mathbf{V}_s\right)\,.\end{aligned} \tag{26}$$

$\mathbf{Res}_s^*$ is also approximated via an Adams-Bashforth method,

$$\mathbf{Res}_s^* \;=\; \frac{3\mathbf{Res}_s^n - \mathbf{Res}_s^{n-1}}{2}\,. \tag{27}$$

In other words, in the predictor stage of the proposed algorithm, the Newtonian component of the granular viscous stresses is integrated via a semi-implicit Crank-Nicolson scheme, whereas the non-Newtonian component is integrated via an explicit Adams-Bashforth method.

In order to avoid the inversion of the nonlinear equation (25), we employ a fractional projection which amounts to introducing provisional velocities. More specifically, the provisional granular velocity $\tilde{\boldsymbol{u}}_s$ is defined as follows,

$$\phi_s^*\tilde{\boldsymbol{u}}_s - L_s \;=\; \phi_s^n\boldsymbol{u}_s^n + R_s + \Delta t\,\mathbf{Res}_s^*\,, \tag{28}$$

where the quantities L_s and R_s are given by

$$L_s \;=\; \frac{\Delta t}{\rho_s \mathrm{Re}}\nabla\cdot\left(\mu_s^*\phi_s^*\tilde{\mathbf{V}}_s^{\mathrm{d}}\right) + \frac{\Delta t}{2\rho_f \mathrm{Re}}\nabla\cdot\left(\zeta_f^*\phi_f^*(\nabla\cdot\tilde{\boldsymbol{u}}_s)\mathbf{I}\right)\,, \tag{29}$$

and

$$R_s \;=\; \frac{\Delta t}{\rho_s \mathrm{Re}}\nabla\cdot\left(\mu_s\phi_s\mathbf{V}_s^{\mathrm{d}}\right)^n + \frac{\Delta t}{2\rho_s \mathrm{Re}}\nabla\cdot\left(\zeta_s\phi_s\,(\nabla\cdot\boldsymbol{u}_s)\,\mathbf{I}\right)^n\,, \tag{30}$$

respectively. From equation (28) it can be inferred that the proposed algorithm belongs to the class of the so-called *pressure-free* methods.

3) Subsequently, we perform to the projection step. To this end, we rewrite the discretized momentum equation (25) in terms of the provisional granular velocity $\tilde{\boldsymbol{u}}_s$. The result is

$$\phi_s^*\tilde{\boldsymbol{u}}_s \;=\; \phi_s^*\boldsymbol{u}_s^* + \frac{\Delta t}{\rho_s}\nabla p_d^* - \Delta t\frac{\rho_s-\rho_f}{\rho_s}\phi_s^*\boldsymbol{g}\,. \tag{31}$$

We remark that the gravity term appears at the right-hand side equation (31). This might come as a surprise because in the literature of projection methods this term is typically incorporated in the computation of the provisional velocity $\tilde{\boldsymbol{u}}_s$. Our choice is motivated by the fact that it allows for a seamless implementation of boundary conditions; see also the relevant discussion in [35].

The predicted values of the auxiliary pressure p_d^* are computed as the solution to the elliptic equation that arises upon taking the divergence of (31). This requires the computation of the term $\nabla\cdot(\phi_s^*\boldsymbol{u}_s^*)$ which, by virtue of the continuity equation for the granular phase (19), is equal to $\left(\frac{\partial\phi_s}{\partial t}\right)^*$. In principle, this time derivative can be approximated via backward differencing. This approach has been successfully applied in developing projection methods for single-phase variable-density flows [32, 38]. However, as it turned out, in our case this approach led to detrimental numerical instabilities. A more efficient approach is to approximate this time derivative from the compaction equation (21) as follows,

$$\left(\frac{\partial\phi_s}{\partial t}\right)^* \;\approx\; \mathrm{Re}\frac{\rho_s\,\phi_f^*}{\mu_c\,\Delta t}\,p_d^* + \mathrm{Re}\frac{\rho_s\,\phi_s^*\phi_f^*}{\mu_c\,\Delta t}\,(-\beta_s^* + \nabla\cdot\,(\gamma_s^*\nabla\phi_s^*)) - \boldsymbol{u}_s^n\nabla\phi_s^*\,. \tag{32}$$

Then, we can derive an equation for p_d^* by taking the divergence of (31) and by inserting (32) into the resulting expression. This operation amounts to projecting the momentum equation for the granular phase (19) on the subspace of velocity fields whose divergence is given by (15). The final result is a second-order elliptic equation for p_d^* that reads

$$\nabla^2 p_d^* - \mathrm{Re}\frac{\rho_s\,\phi_f^*}{\mu_c\,\Delta t}\;p_d^* \;=\; \mathrm{Re}\frac{\rho_s\,\phi_s^*\phi_f^*}{\mu_c\,\Delta t}\;(-\beta_s^* + \nabla\cdot\,(\gamma_s^*\nabla\phi_s^*)) + (\rho_s-\rho_f)\boldsymbol{g}\cdot\nabla\phi_s^* + \frac{\rho_s}{\Delta t}\nabla\cdot(\phi_s^*\tilde{\boldsymbol{u}}_s) + \boldsymbol{u}_s^n\nabla\phi_s^*\,. \tag{33}$$

The auxiliary pressure p_d^* can be evaluated by discretizing (33) and solving the resulting linear system. Once p_d^* has been computed, the predicted value of the granular velocity, $\boldsymbol{u}_s^*$, can be obtained directly from (31).

4) Next, the momentum equation for the fluid phase (18) is discretized in a similar manner,

$$\frac{\phi_f^* \boldsymbol{u}_f^* - \phi_f^n \boldsymbol{u}_f^n}{\Delta t} + \frac{\phi_f^{n+1}}{\rho_f} \nabla p_f'^* = \frac{1}{\rho_f \mathrm{Re}} \nabla\cdot \left(\left(\mu_f \phi_f \mathbf{V}_f^{\mathrm{d}} \right)^* + \left(\mu_f \phi_f \mathbf{V}_f^{\mathrm{d}} \right)^n \right) + \frac{1}{2\rho_f \mathrm{Re}} \nabla\cdot \left(\left(\zeta_f \phi_f \nabla\cdot \boldsymbol{u}_f \right)^* \mathbf{I} + \left(\zeta_f \phi_f \nabla\cdot \boldsymbol{u}_f \right)^n \mathbf{I} \right) + \mathbf{Res}_f^* , \tag{34}$$

where the residual $\mathbf{Res}_f$ is defined as

$$\mathbf{Res}_f = -\nabla\cdot (\phi_f \mathbf{u}_f \otimes \mathbf{u}_f) - \frac{\delta}{\rho_f} (\boldsymbol{u}_f - \boldsymbol{u}_s) , \tag{35}$$

and it is also integrated via an Adams-Bashforth scheme,

$$\mathbf{Res}_f^* = \frac{3\mathbf{Res}_f^n - \mathbf{Res}_f^{n-1}}{2} . \tag{36}$$

The provisional fluid velocity $\tilde{\boldsymbol{u}}_f$ is defined as

$$\phi_f^* \tilde{\boldsymbol{u}}_f - L_f = \phi_f^n \boldsymbol{u}_f^n + R_f + \Delta t \, \mathbf{Res}_f^* \tag{37}$$

where L_f and R_f are given by

$$L_f = \frac{\Delta t}{\rho_f \mathrm{Re}} \nabla\cdot \left(\mu_f^* \phi_f^* \tilde{\mathbf{V}}_f^{\mathrm{d}} \right) + \frac{\Delta t}{2\rho_f \mathrm{Re}} \nabla\cdot \left(\zeta_f^* \phi_f^* (\nabla\cdot \tilde{\boldsymbol{u}}_f) \mathbf{I} \right) , \tag{38}$$

and

$$R_f = \frac{\Delta t}{\rho_f \mathrm{Re}} \nabla\cdot \left(\mu_f \phi_f \mathbf{V}_f^{\mathrm{d}} \right)^n + \frac{\Delta t}{2\rho_f \mathrm{Re}} \nabla\cdot \left(\zeta_f \phi_f \left(\nabla\cdot \boldsymbol{u}_f \right) \mathbf{I} \right)^n , \tag{39}$$

respectively. Herein, $\tilde{\mathbf{V}}_f^{\mathrm{d}}$ is computed on the basis of the provisional velocities $\tilde{\boldsymbol{u}}_f$.

5) The projection step for the fluid phase takes the form,

$$\phi_f^* \tilde{\boldsymbol{u}}_f = \phi_f^* \boldsymbol{u}_f^* + \Delta t \frac{\phi_f^*}{\rho_f} \nabla p'^*_f , \tag{40}$$

By virtue of equations (17) and (19), the term $\nabla\cdot (\phi_s \boldsymbol{u}_f)$ must satisfy the following condition,

$$\nabla\cdot (\phi_f^* \boldsymbol{u}_f^*) = -\nabla\cdot (\phi_s^* \boldsymbol{u}_s^*). \tag{41}$$

Since the value $\boldsymbol{u}_s^*$ has already been computed, then equation (41) can be used to evaluate the fluid auxiliary pressure. More specifically, by taking the divergence of (40) and upon inserting (41) into it, we arrive at the following elliptic PDE for the predicted value of p'_f,

$$\nabla\cdot (\phi_f^* \nabla p_f'^*) = \frac{\rho_f}{\Delta t} \nabla\cdot (\phi_f^* \tilde{\boldsymbol{u}}_f) + \frac{\rho_f}{\Delta t} \nabla\cdot (\phi_s^* \boldsymbol{u}_s^*) . \tag{42}$$

Then, p'^*_f is evaluated by discretizing the above equation and solving the resulting linear system. Subsequently, the predicted fluid velocity $\boldsymbol{u}_f^*$ is computed directly from (40), which concludes the predictor stage of the time-marching iteration step.

3.2.2. Corrector stage

1) The value of the volume fraction at $(n+1)\Delta t$, ϕ_s^{n+1}, is computed from the compaction equation (21) as follows,

$$\frac{\phi_s^{n+1}-\phi_s^n}{\Delta t} = \mathrm{Re}\frac{\phi_s^{n+1/2}\phi_f^{n+1/2}}{\mu_c}\nabla\cdot\left(\frac{\gamma_s^{n+1/2}}{2}\left(\nabla\phi_s^{n+1}+\nabla\phi_s^n\right)\right)+\mathrm{Res}_\phi^{n+1/2}\,. \tag{43}$$

In the above equation, the terms with index $n+1/2$ are computed as averages between their values at $n\Delta T$ and their values computed in the predictor stage, e.g. $\phi_s^{n+1/2}=\frac{1}{2}(\phi_s^*+\phi_s^n)$ and $\mathrm{Res}_\phi^{n+1/2}=\frac{1}{2}\left(\mathrm{Res}_\phi^*+\mathrm{Res}_\phi^n\right)$.

2) Next, the momentum equation for the granular phase is discretized as

$$\begin{aligned}\frac{\phi_s^{n+1}\boldsymbol{u}_s^{n+1}-\phi_s^n\boldsymbol{u}_s^n}{\Delta t}+\frac{1}{\rho_s}\nabla p_d^{n+1} &= \frac{1}{\rho_s\mathrm{Re}}\nabla\cdot\left(\left(\mu_{s1}\phi_s\mathbf{V}_s^{\mathrm{d}}\right)^{n+1}+\left(\mu_{s1}\phi_s\mathbf{V}_s^{\mathrm{d}}\right)^n\right)\\ &\quad\frac{1}{2\rho_s\mathrm{Re}}\nabla\cdot\left(\left(\zeta_{s1}\phi_s\nabla\cdot\boldsymbol{u}_s\right)^{n+1}\mathbf{I}+\left(\zeta_{s1}\phi_s\nabla\cdot\boldsymbol{u}_s\right)^n\mathbf{I}\right)+\\ &\quad\mathbf{Res}_s^{n+1/2}+\frac{\rho_s-\rho_f}{\rho_s}\phi_s^{n+1}\boldsymbol{g}\,,\end{aligned} \tag{44}$$

where $\mathbf{Res}_s^{n+1/2}=\frac{1}{2}(\mathbf{Res}_s^*+\mathbf{Res}_s^n)$.

Then, the provisional velocity of the granular phase for the corrector stage $\breve{\boldsymbol{u}}_s$ is defined as

$$\phi_s^{n+1}\breve{\boldsymbol{u}}_s-L_s = \phi_s^n\boldsymbol{u}_s^n+R_s+\Delta t\,\mathbf{Res}_s^{n+1/2}\,, \tag{45}$$

with

$$L_s = \frac{\Delta t}{\rho_s\mathrm{Re}}\nabla\cdot\left(\mu_s^{n+1}\phi_s^{n+1}\breve{\mathbf{V}}_s^{\mathrm{d}}\right)+\frac{\Delta t}{2\rho_f\mathrm{Re}}\nabla\cdot\left(\zeta_f^{n+1}\phi_f^{n+1}(\nabla\cdot\breve{\boldsymbol{u}}_s)\mathbf{I}\right)\,, \tag{46}$$

$$R_s = \frac{\Delta t}{\rho_s\mathrm{Re}}\nabla\cdot\left(\mu_s\phi_s\mathbf{V}_s^{\mathrm{d}}\right)^n+\frac{\Delta t}{2\rho_s\mathrm{Re}}\nabla\cdot\left(\zeta_s\phi_s\left(\nabla\cdot\boldsymbol{u}_s\right)\mathbf{I}\right)^n\,. \tag{47}$$

Also, $\breve{\mathbf{V}}_s^{\mathrm{d}}$ is computed on the basis of the provisional velocities $\breve{\boldsymbol{u}}_s$.

3) Subsequently, we perform the projection step for the momentum equation of the granular phase which reads

$$\phi_s^{n+1}\breve{\boldsymbol{u}}_s = \phi_s^{n+1}\boldsymbol{u}_s^{n+1}+\frac{\Delta t}{\rho_s}\nabla p_d^{n+1}-\Delta t\frac{\rho_s-\rho_f}{\rho_s}\phi_s^{n+1}\boldsymbol{g}\,. \tag{48}$$

The auxiliary pressure p_d^{n+1} is computed as the solution to the elliptic equation that arises upon taking the divergence of (48). By virtue of the continuity equation of the granular phase, the divergence of the first term in the left-hand side of (48) is equal to $\left(\frac{\partial\phi_s}{\partial t}\right)^{n+1}$. As in the predictor stage, this derivative is computed via the compaction equation (21). The divergence of (48) yields the following elliptic equation for p_d^{n+1},

$$\begin{aligned}\nabla^2 p_d^{n+1}-\mathrm{Re}\frac{\rho_s\,\phi_f^{n+1}}{\mu_c\,\Delta t}\,p_d^{n+1} &= \mathrm{Re}\frac{\rho_s\,\phi_s^{n+1}\phi_f^{n+1}}{\mu_c\,\Delta t}\left(-\beta_s^{n+1}+\nabla\cdot(\gamma_s^{n+1}\nabla\phi_s^{n+1})\right)\\ &\quad+(\rho_s-\rho_f)\nabla\phi_s^{n+1}\cdot\boldsymbol{g}+\frac{\rho_s}{\Delta t}\nabla\cdot(\phi_s^{n+1}\breve{\boldsymbol{u}}_s)+\boldsymbol{u}_s^*\nabla\phi_s^{n+1}\,.\end{aligned} \tag{49}$$

The auxiliary pressure p_d^{n+1} is evaluated by discretizing (49) and solving the resulting linear system. Once p_d^{n+1} has been computed, the updated value of the granular velocity, $\boldsymbol{u}_s^{n+1}$, can be obtained directly from (48).

4) Next, the momentum equation for the fluid phase (18) is discretized in an similar manner,

$$\frac{\phi_f^{n+1}\boldsymbol{u}_f^{n+1}-\phi_f^n\boldsymbol{u}_f^n}{\Delta t}+\frac{\phi_f^{n+1}}{\rho_f}\nabla p_f'^{n+1/2} = \frac{1}{\rho_f \mathrm{Re}}\nabla\cdot\left(\left(\mu_f\phi_f\mathbf{V}_f^{\mathrm{d}}\right)^{n+1}+\left(\mu_f\phi_f\mathbf{V}_f^{\mathrm{d}}\right)^{n}\right) + \frac{1}{2\rho_f \mathrm{Re}}\nabla\cdot\left(\left(\zeta_f\phi_f\nabla\cdot\boldsymbol{u}_f\right)^{n+1}\mathbf{I}+\left(\zeta_f\phi_f\nabla\cdot\boldsymbol{u}_f\right)^{n}\mathbf{I}\right) + \mathbf{Res}_f^{n+1/2}, \tag{50}$$

where $\mathbf{Res}_f^{n+1/2} = \frac{1}{2}(\mathbf{Res}_f^{*}+\mathbf{Res}_f^{n})$.

The provisional fluid velocity $\check{\boldsymbol{u}}_f$ is computed as follows,

$$\phi_f^{n+1}\check{\boldsymbol{u}}_f - L_f = \phi_f^n\boldsymbol{u}_f^n + R_f + \Delta t\,\mathbf{Res}_f^{n+1/2} \tag{51}$$

where L_f and R_f are now given by

$$L_f = \frac{\Delta t}{\rho_f \mathrm{Re}}\nabla\cdot\left(\mu_f^{n+1}\phi_f^{n+1}\check{\mathbf{V}}_f^{\mathrm{d}}\right)+\frac{\Delta t}{2\rho_f \mathrm{Re}}\nabla\cdot\left(\zeta_f^{n+1}\phi_f^{n+1}(\nabla\cdot\check{\boldsymbol{u}}_f)\mathbf{I}\right), \tag{52}$$

$$R_f = \frac{\Delta t}{\rho_f \mathrm{Re}}\nabla\cdot\left(\mu_f\phi_f\mathbf{V}_f^{\mathrm{d}}\right)^{n}+\frac{\Delta t}{2\rho_f \mathrm{Re}}\nabla\cdot\left(\zeta_f\phi_f\left(\nabla\cdot\boldsymbol{u}_f\right)\mathbf{I}\right)^{n}. \tag{53}$$

$$\tag{54}$$

5) The projection step for the fluid phase reads,

$$\phi_f^{n+1}\check{\boldsymbol{u}}_f = \phi_f^{n+1}\boldsymbol{u}_f^{n+1}+\Delta t\frac{\phi_f^{n+1}}{\rho_f}\nabla p_f'^{n+1}, \tag{55}$$

By virtue of equations (17) and (19), the term $\nabla\cdot(\phi_s\boldsymbol{u}_f)$ must satisfy the following condition,

$$\nabla\cdot(\phi_f^{n+1}\boldsymbol{u}_f^{n+1}) = -\nabla\cdot(\phi_s^{n+1}\boldsymbol{u}_s^{n+1}). \tag{56}$$

Since the value $\boldsymbol{u}_s^{n+1}$ has already been computed, then equation (56) can be used to evaluate the fluid auxiliary pressure. More specifically, by taking the divergence of (55) and upon inserting (56) into it, we arrive at the following elliptic PDE for $p_f'^{n+1}$,

$$\nabla\cdot(\phi_f^{n+1}\nabla p_f'^{n+1}) = \frac{\rho_f}{\Delta t}\nabla\cdot(\phi_f^{n+1}\check{\boldsymbol{u}}_f)+\frac{\rho_f}{\Delta t}\nabla\cdot(\phi_s^{n+1}\boldsymbol{u}_s^{n+1}). \tag{57}$$

Then, $p_f'^{n+1}$ is evaluated by discretizing the above equation and solving the resulting linear system. Subsequently, the fluid velocity $\boldsymbol{u}_f^{n+1}$ is computed directly from (55), which concludes the time-marching iteration step.

3.3. Boundary conditions

The afore-described algorithm requires that not only the volume fraction ϕ_s but also the provisional velocities $\tilde{\boldsymbol{u}}_a$ and $\check{\boldsymbol{u}}_a$ be endowed with appropriate boundary conditions. From a numerical perspective, the assignment of boundary condition for ϕ_s is not of particular concern because the governing equation for ϕ_s, i.e. the compaction equation (21), is of the advection-diffusion type.

On the other hand, it is well established, see e.g. [39], that the assignment of boundary conditions for the provisional velocity of the Navier-Stokes equations is crucial for enforcing correct boundary conditions for the tangential velocity component and for preserving second-order accuracy for the pressure field. The same is expected to hold true for two-phase flow models as well. An application of the analysis of [39] to equations (17) – (21) suggests that the tangential components of the provisional velocities be assigned the following boundary conditions,

$$\tilde{\boldsymbol{u}}_s|_{\partial\Omega}\cdot\boldsymbol{\tau} = \boldsymbol{u}_s^{*}|_{\partial\Omega}\cdot\boldsymbol{\tau}+\frac{\Delta t}{\rho_s\phi_s^{*}}\nabla p_d^{*}|_{\partial\Omega}\cdot\boldsymbol{\tau}-\Delta t\frac{\rho_s-\rho_f}{\rho_s}\,\boldsymbol{g}\cdot\boldsymbol{\tau}, \tag{58}$$

$$\tilde{\boldsymbol{u}}_f|_{\partial\Omega}\cdot\boldsymbol{\tau} = \boldsymbol{u}_f^{*}|_{\partial\Omega}\cdot\boldsymbol{\tau}+\frac{\Delta t}{\rho_f}\nabla p_f'^{*}|_{\partial\Omega}\cdot\boldsymbol{\tau}, \tag{59}$$

and, similarly,

$$\check{\boldsymbol{u}}_s^{n+1}|_{\partial\Omega}\cdot\boldsymbol{\tau} = \boldsymbol{u}_s^{n+1}|_{\partial\Omega}\cdot\boldsymbol{\tau} + \frac{\Delta t}{\rho_s\phi_s^{n+1}}\nabla p_d^{n+1}|_{\partial\Omega}\cdot\boldsymbol{\tau} - \Delta t\frac{\rho_s-\rho_f}{\rho_s}\,\boldsymbol{g}\cdot\boldsymbol{\tau}\,, \tag{60}$$

$$\check{\boldsymbol{u}}_f^{n+1}|_{\partial\Omega}\cdot\boldsymbol{\tau} = \boldsymbol{u}_f^{n+1}|_{\partial\Omega}\cdot\boldsymbol{\tau} + \frac{\Delta t}{\rho_f}\nabla p_f'^{n+1}|_{\partial\Omega}\cdot\boldsymbol{\tau}\,, \tag{61}$$

where $\partial\Omega$ denotes the boundary of the domain Ω and $\boldsymbol{\tau}$ is a unit vector tangent to the boundary. In fact, the pair of equations (58) and (59) are simply the tangential components of (31) and (40), respectively. The same is true for the pair (60) and (61).

The quantities $\boldsymbol{u}_s^*|_{\partial\Omega}\cdot\boldsymbol{\tau}$, $\boldsymbol{u}_f^*|_{\partial\Omega}\cdot\boldsymbol{\tau}$, $\boldsymbol{u}_s^{n+1}|_{\partial\Omega}\cdot\boldsymbol{\tau}$ and $\boldsymbol{u}_f^{n+1}|_{\partial\Omega}\cdot\boldsymbol{\tau}$ are known from the boundary conditions for the velocity fields. The quantities ϕ_s^* and ϕ_s^{n+1} are also known during step 2 of the predictor and corrector stages, because they have been computed in step 1 of each stage. However, p_d^*, $p_f'^*$, p_d^{n+1} and $p_f'^{n+1}$ are not known at this stage of the algorithm and, therefore, they need to be approximated. For the case of the Navier-Stokes equations, Kim and Moin [37] have shown that replacing these values with p_d^n and $p_f'^n$ still results in a second-order-accurate scheme. Motivated by this fact, we opted for the same substitution in our algorithm too. Accordingly, the boundary conditions for the tangential components of $\tilde{\boldsymbol{u}}_s$ and $\tilde{\boldsymbol{u}}_f$ read,

$$\tilde{\boldsymbol{u}}_s|_{\partial\Omega}\cdot\boldsymbol{\tau} = \boldsymbol{u}_{s_b}\cdot\boldsymbol{\tau} + \frac{\Delta t}{\rho_s\phi_s^*}\nabla p_d^n|_{\partial\Omega}\cdot\boldsymbol{\tau} - \Delta t\frac{\rho_s-\rho_f}{\rho_s}\boldsymbol{g}\cdot\boldsymbol{\tau}\,, \tag{62}$$

$$\tilde{\boldsymbol{u}}_f|_{\partial\Omega}\cdot\boldsymbol{\tau} = \boldsymbol{u}_{f_b}\cdot\boldsymbol{\tau} + \frac{\Delta t}{\rho_f}\nabla p'^n_f|_{\partial\Omega}\cdot\boldsymbol{\tau}\,, \tag{63}$$

and, similarly,

$$\check{\boldsymbol{u}}_s|_{\partial\Omega}\cdot\boldsymbol{\tau} = \boldsymbol{u}_{s_b}\cdot\boldsymbol{\tau} + \frac{\Delta t}{\rho_s\phi_s^{n+1}}\nabla p_d^n|_{\partial\Omega}\cdot\boldsymbol{\tau} - \Delta t\frac{\rho_s-\rho_f}{\rho_s}\boldsymbol{g}\cdot\boldsymbol{\tau}\,, \tag{64}$$

$$\check{\boldsymbol{u}}_f|_{\partial\Omega}\cdot\boldsymbol{\tau} = \boldsymbol{u}_{f_b}\cdot\boldsymbol{\tau} + \frac{\Delta t}{\rho_f}\nabla p'^n_f|_{\partial\Omega}\cdot\boldsymbol{\tau}\,. \tag{65}$$

On the other hand, the boundary conditions for the normal components of $\tilde{\boldsymbol{u}}_s$, $\tilde{\boldsymbol{u}}_f$, $\check{\boldsymbol{u}}_s$ and $\check{\boldsymbol{u}}_f$ are inherited from the Helmholtz-Marsden decomposition and, in particular, from the requirement that the decomposition be orthogonal. Therefore, the following boundary conditions are prescribed,

$$\tilde{\boldsymbol{u}}_s|_{\partial\Omega}\cdot\boldsymbol{n} = \check{\boldsymbol{u}}_s|_{\partial\Omega}\cdot\boldsymbol{n} = \boldsymbol{u}_s^{n+1}|_{\partial\Omega}\cdot\boldsymbol{n}\,, \tag{66}$$

$$\tilde{\boldsymbol{u}}_f|_{\partial\Omega}\cdot\boldsymbol{n} = \check{\boldsymbol{u}}_f|_{\partial\Omega}\cdot\boldsymbol{n} = \boldsymbol{u}_f^{n+1}|_{\partial\Omega}\cdot\boldsymbol{n}\,, \tag{67}$$

where $\boldsymbol{n}$ denotes the unit vector normal to the boundary. As regards the boundary conditions for the auxiliary pressures, they are directly deduced by combining (66) and (67) with (31), (40), (48) and (55). This yields the following conditions,

$$\nabla p_d^*|_{\partial\Omega}\cdot\boldsymbol{n} = \phi_s^*(\rho_s-\rho_f)\boldsymbol{g}\cdot\boldsymbol{n}, \tag{68}$$

$$\nabla p_f'^*|_{\partial\Omega}\cdot\boldsymbol{n} = 0\,, \tag{69}$$

and, similarly,

$$\nabla p_d^{n+1}|_{\partial\Omega}\cdot\boldsymbol{n} = \phi_s^{n+1}(\rho_s-\rho_f)\boldsymbol{g}\cdot\boldsymbol{n}, \tag{70}$$

$$\nabla p_f'^{n+1}|_{\partial\Omega}\cdot\boldsymbol{n} = 0\,, \tag{71}$$

In other words, the auxiliary pressures for the two phases are endowed with different Neumann conditions.

Finally, it is important to mention that since p_d satisfies (33), which is an inhomogeneous linear elliptic equation, it is determined exactly and not up to an additive constant. This is an important element for the accurate integration of the compaction equation for ϕ_s. On the other hand, p_f' satisfies the homogeneous elliptic equation (42) and, therefore, it is determined up to an additive constant. Nonetheless, the value of this constant is inconsequential because it can be absorbed by the gravity term that enters the definition (16) of p_f'.

3.4. Spatial discretization

In the proposed algorithm, spatial discretization of all linear diffusive fluxes is performed via second-order, centered finite differences with linear interpolation of the material properties inside the computational cells. Further, the tensor $\mathbf{C}_s$ that is defined in given by (10) and describes Korteweg-type stresses acting on the granular phase, is also discretized via second-order centered differences.

For the discretization of the nonlinear part of the granular viscous stress tensor $\mathbf{T}_s$, which enters the expression for the residual $\mathbf{Res}_s$ in equation (25), we proceed as follows. Let $\mathbf{T}_{sn}$ denote the nonlinear part of $\mathbf{T}_s$. Then, according to (11),

$$\mathbf{T}_{sn} \;=\; (\zeta_{s2}\nabla\cdot\boldsymbol{u}_s + \chi_1)\phi_s\mathbf{I} + 2\mu_{s2}\phi_s\mathbf{V}_s^{\mathrm{d}} + \chi_2\phi_s\mathbf{V}_s\cdot\mathbf{V}_s\,. \tag{72}$$

Now let a_i, $i = 1, 2, 3$ denote the following invariants of $\mathbf{V}_s$

$$a_1 \;=\; \mathrm{tr}\mathbf{V}_s\,, \quad a_2 \;=\; \mathbf{V}_s : \mathbf{V}_s\,, \quad a_3 \;=\; \det\mathbf{V}_s. \tag{73}$$

Then, equation (72) can be written in terms of these invariants, which yields

$$\mathbf{T}_{sn} \;=\; \left(\frac{\sqrt{2}}{3}\frac{a_3}{a_2^{3/2}}\nabla\cdot\boldsymbol{u}_s + \frac{3a_2 - a_1^2}{\sqrt{2a_2}} - 2\sqrt{2}\sqrt{a_2 - \frac{a_1^2}{3}}\right)\mathbf{I} + \sqrt{2}\frac{a_3}{a_2^{3/2}}\mathbf{V}_s^{\mathrm{d}} - \sqrt{\frac{2}{a_2}}\mathbf{V}_s\cdot\mathbf{V}_s. \tag{74}$$

In the proposed algorithm the invariants a_1, a_2, and a_3 are first computed at cells centers via second-order centered differences and subsequently they are linearly interpolated at cell interfaces. On the other hand, the components of $\mathbf{V}_s$ and $\mathbf{V}_s^{\mathrm{d}}$, as well as the velocity divergence, are computed directly via second-ordered centered differences at cell interfaces. It is also worth noting that, as elaborated in [12], all five components of $\mathbf{T}_s^n$ vanish as $\mathbf{V}_s \to 0$. Numerically, this is remedied with the addition a very small value, e.g. $\varepsilon = 10^{-12}$, to the denominator of each component.

The proposed algorithm is discretized via finite differences on a collocated grid. Their advantages over staggered grids are computational simplicity and straightforward extension of the method to curvilinear coordinate systems. On the other hand, it is well-known that collocated grids can produce spurious oscillations of the pressure field; this is the well documented "odd-even decoupling" problem. Rhie and Chow [40] first addressed this problem by proposing a flux-interpolation technique. Since then, several authors presented modified versions of this technique that offer increased robustness; see, for example, [40–44]. According to this procedure, the convective fluxes at the cell interfaces are computed by combining values of the velocity, volume fractions, and the gradients of the pressure. Our algorithm is endowed with such a technique, which is described in detail in the Appendix.

Finally, with regard to the compaction equation (21), the discretization of the advection term in (23) should be robust enough to handle steep gradients of ϕ_s that commonly occur across interfaces. This can be accomplished via an upwind scheme such as the Corner-Transport-Upwind (CTU) algorithm of Colella [45]. Moreover, the large variation of ϕ_s across interfaces renders the mass and momentum balance laws (17) – (20) stiff, which may trigger numerical instabilities. The control of such instabilities is achieved via the application of an interface-regularization scheme. The basic idea behind this scheme is to replace the values of ϕ_s in the vicinity of steep gradients by the values of a smoother, and preferably compactly supported, function [46, 47]. In the proposed algorithm, we employ a simple parabolic regularization after the time integration of the compaction equation. This procedure is outlined in the Appendix; for more details, the interested reader is referred to [35].

3.5. A note on the coupling between the compaction and momentum equations

As already mentioned above, the momentum equation of the granular phase (20) is strongly coupled to the compaction equation (14) because the difference between the pressures of the two phases, $p_s - p_f$, appears as a source term therein. This coupling has a profound impact on the performance of the numerical method, which can be exemplified by the approximation of the time derivative $\frac{\partial\phi}{\partial t}$ during the projection step, i.e. the discretization of the divergence of (20). In fact, it has long been recognized that errors in the approximation of this derivative have an important destabilising effect in projection-based algorithms for variable-density or two-phase flows; see [32] and references therein. The ramifications of the coupling between equations (20) and (21) can be illustrated with the following example.

We consider the following system that is a simplified version of the compaction equation and the elliptic equation for p_d that results from the projection step of the momentum equation of the granular phase, cf. (33),

$$\frac{\partial \omega}{\partial t} = c_1 \left(q - c_2 \omega + \nabla \cdot (c_3 \nabla \omega) \right) , \tag{75}$$

$$\nabla^2 q = \frac{1}{\epsilon} \frac{\partial \omega}{\partial t} . \tag{76}$$

In these equations, c_1, c_2, and c_3, are positive constants and ϵ is a small positive constant. The variables ω and q play the role of surrogate volume fraction and phasial-pressure difference (ϕ_s and p_d), respectively. It can be shown that if one approximates the time derivative $\frac{\partial \omega}{\partial t}$ in both (75) and (76) via backward Euler,

$$\omega^{n+1} = \omega^n + \Delta t \, c_1 \left(q^n - c_2 \omega^n + \nabla \cdot (c_3 \nabla \omega^n) \right) , \tag{77}$$

$$\nabla^2 q^{n+1} = \frac{1}{\epsilon} \frac{\omega^{n+1} - \omega^n}{\delta t} , \tag{78}$$

then the algorithm is unstable [48].

On the other hand, one can apply a procedure that mimics the algorithm for granular suspensions that was described above. This amounts to integrating (75) via backward Euler but substituting the right-hand side of (75) into (76), i.e.

$$\omega^{n+1} = \omega^n + \Delta t \, c_1 \left(q^n - c_2 \omega^n + \nabla \cdot (c_3 \nabla \omega^n) \right) , \tag{79}$$

$$\nabla^2 q^{n+1} - \frac{1}{\epsilon} \Delta t \, c_1 \, q^{n+1} = \frac{1}{\epsilon} \Delta t \, c_1 \left(-c_2 \omega^n + \nabla \cdot (c_3 \nabla \omega^n) \right) . \tag{80}$$

It can be shown that this algorithm has much improved properties: [48]. This result suggests that the coupling between the compaction and momentum equations has to be treated with particular care and that stopgap approaches will most likely result in unsatisfactory performance of the algorithm.

4. Numerical results

In this section we present and discuss results for three numerical tests that we conducted in order to assess the performance of the proposed algorithm. These tests involve sand-water mixtures and concern: i) sedimentation of a granular suspension, ii) compaction of a dense sediment bed, and iii) collapse of a submerged granular column. The proposed algorithm has been implemented in a 3D parallel code written in C/C++ and uses the PETSc suite of data structures and routines for the scalable solution of PDEs [49]. Parallelization is performed via Message Passing Interface (MPI). In particular, the linear systems resulting from the discretization of the elliptic equations (33), (42), (49) and (57) are solved with the PETSc routine for the Biconjugate Gradient Stabilized (BiCGstab) method with Jacobi preconditioning and MPI. The simulations have been performed in a computer equipped with 4 Intel® Xeon® E7-4820v3 processors (totalling 40 cores) and with 16 DD3-1600-ECC memory modules of 8Gb each.

4.1. Physical parameters

Below we present the physical parameters for the mixture under study and the correlations for the various material and transport coefficients that we used in our computations. The hat symbol $\hat{}$ is used to denote dimensional quantities.

We consider a monodispersed granular suspension of sand in water. The grain diameter is $\hat{d}_p = 3.5 \times 10^{-4}$ m and the maximum packing of grains is $\phi_m = 0.6$. The mass density of the fluid phase is $\hat{\rho}_f = 1000\,\mathrm{kg/m^3}$, while the density of the granular phase is $\hat{\rho}_s = 2500\,\mathrm{kg/m^3}$. The gravitational acceleration is $|\hat{\boldsymbol{g}}| = 9.81\,\mathrm{m/s^2}$. For the interphasial drag coefficient $\hat{\delta}$, the HKL-type correlation proposed in [50] is employed, which is applicable over a wide range of volume fractions and Reynolds numbers. According to this correlation, the coefficient $\hat{\delta}$ is given as a function of the local volume fraction ϕ_s, the particle diameter $\hat{d}_p$ and the particle Reynolds number Re_p (which is defined in terms of $\hat{d}_p$, $\hat{\rho}_f$, $\hat{\mu}_f$ and the slip velocity $\|\hat{\boldsymbol{u}}_f - \hat{\boldsymbol{u}}_s\|$),

$$\hat{\delta} = f(\phi_s, \hat{d}_p, \mathrm{Re}_p) . \tag{81}$$

The exact expression for (81) is too long and cumbersome to reproduce herein, comprising several cases and containing various numerical constants. For a code-friendly description of the correlation, the interested reader is referred to [50].

As regards β_s and γ_s, we first remark that since they are properties of the granular phase, then their constitutive relations have to be derived via experimental measurements. Also, since they relate to the microstructure of the granular phase, their constitutive relations should depend on the parameters that characterize this microstructure. Further, since the intergranular stress $\hat{\beta}_s$ expresses the resistance of solid particles to compaction, it is expected to vanish for small values of ϕ_s [51] and to diverge at ϕ_m [52]. In our study we employed the following expression, which is a simplified version of the relation proposed in [53],

$$\hat{\beta}_s \;=\; -\hat{\beta}_0 \log\left(\frac{\phi_m - \phi_s}{\phi_m}\right), \quad \hat{\beta}_0 \;=\; 0.1\,\text{Pa}. \tag{82}$$

The coefficient $\hat{\beta}_0$ also depends on the microstructure of the particulate phase. The above value of $\hat{\beta}_0$ has been calibrated with respect to the experimental data in [54] for pressure-driven flows of suspensions containing spherical particles.

On the other hand, experimental measurements for $\hat{\gamma}_s$ are particular scarce. Nonetheless, it is expected to vanish for small values of ϕ_s. Moreover, since it is a thermodynamic derivative, it has to increase monotonically with ϕ_s in order to satisfy the convexity requirement for stability of equilibrium states of the granular medium, [23]. In our study, and due to lack of available experimental data, we opted for a simple power law, namely,

$$\hat{\gamma}_s \;=\; -\hat{\gamma}_0\,\phi_s^6, \quad \hat{\gamma}_0 \;=\; 1.2\times 10^{-4}\,\text{N}. \tag{83}$$

The sixth-power law has been chosen because, as elaborated in [19] it gave better agreement of the calculations reported in [19] for pressure-driven suspensions with the corresponding experimental data of [54]. In the literature various studies are available that employ expressions that diverge at ϕ_m [51, 55, 56]. However, in our study we refrained from adopting the later approach due to absence of conclusive evidence regarding the behaviour of $\hat{\gamma}_s$ near the point of jamming transition.

With regard to viscosity coefficients, the shear and bulk viscosities of water are set at $\hat{\mu}_f = 8.9\times 10^{-4}$ Pa and $\hat{\zeta}_f = 2.7\times 10^{-3}$ Pa, respectively [57]. At this point it is worth remarking that since the fluid velocity is not divergence-free, the bulk viscous forces acting on the fluid phase cannot be ignored. For the viscosity coefficients $\hat{\mu}_{s1}$ and $\hat{\mu}_n$, we employ the following correlations that are based on the formulation proposed in [8],

$$\hat{\mu}_{s1} = \hat{\mu}_f\left(\frac{2.5}{\phi_m - \phi_s} + 0.1\,\frac{\phi_s}{(\phi_m - \phi_s)^2}\right), \tag{84}$$

$$\hat{\mu}_n = 0.75\hat{\mu}_f\,\frac{\phi_s}{(\phi_m - \phi_s)^2}\,. \tag{85}$$

Experimental correlations for the viscosity coefficient $\hat{\zeta}_{s1}$ are also scarce since this quantity is difficult to measure. Nonetheless, it is expected that $\hat{\zeta}_{s1}$ depends on ϕ_s similarly to $\hat{\mu}_{s1}$; see the relevant discussion in [58]. In the present work, and for simplicity purposes, we assume that $\hat{\zeta}_{s1}$ and $\hat{\mu}_{s1}$ remain proportional, $\hat{\zeta}_{s1} = k\hat{\mu}_{s1}$, and we set the proportionality constant $k = 22.5$.

Finally, one must provide an expression for the compaction viscosity $\hat{\mu}_c$ that enters the particle-migration model, i.e the compaction equation (21). Once again, very little information about this coefficient is available. Upon comparison of available particle-migration models, we may infer that for sufficiently low particle-Reynolds number Re_p, $\hat{\mu}_c$ scales with $\hat{\mu}_f$. For this reason, and in absence of additional information, in the present work we set $\hat{\mu}_c = \hat{\mu}_f$.

4.2. Sedimentation of a granular suspension

The first test case concerns the sedimentation of an initially homogeneous suspension in a vertical tube. As the granular phase moves downward due to gravity, it forms a dense granular bed at the bottom of the tube and leaves a pure-fluid layer above the suspension. In other words, the sedimentation process gives rise to two sharp interfaces. The first one is between the bed and the suspension, and moves upward during the sedimentation. The second one is between the suspension and the pure fluid on top, and moves downward. Due to its conceptual simplicity, this case is

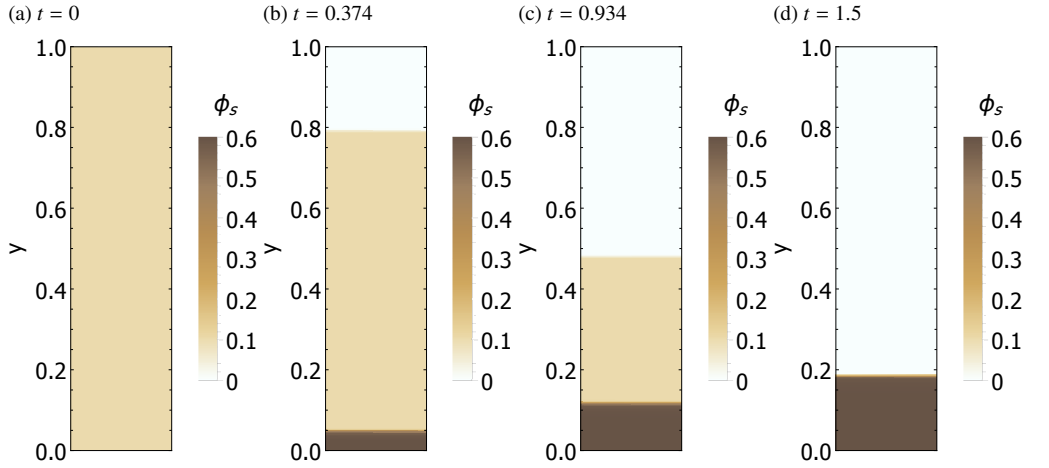

Fig. 1. Sedimentation of a granular suspension: granular volume fraction at different time instances, as computed on a grid of 1024 points. We can readily observe that as the granular phase settles down due to gravity, three different regions are formed: a dense sediment bed at the bottom, a pure-fluid layer at the top and the granular suspension in between.

a convenient test for assessing the capacity of the algorithm to handle steep volume-fraction gradients and flows with significant velocity divergence.

As regards the numerical set up, the suspension is initially homogeneous with $\phi_s = 0.1$ and fills completely a tube whose height is equal to $\hat{h} = 0.4$ m. Also, both fluid and granular phases are initially at rest. The stratification being stable, we approximate the sedimentation process as an one-dimensional process. The bottom boundary of the domain is a rigid wall and, therefore, we apply zero Dirichlet conditions for the phasial velocities and zero Neumann conditions for the phasial pressures and volume fraction. On the other hand, the top boundary is supposed to be open and we apply zero-Neumann condition for the phasial velocities and pressures, and a Dirichlet condition for the volume fraction, $\phi_s = 10^{-5}$. This small value of ϕ_s is an approximation of the pure-fluid limit $\phi_s \to 0$ and is introduced to circumvent the singularities of the governing equations when ϕ_s vanishes.

The reference length of the problem is the height of the computational domain $\hat{h}$. The reference velocity is the sedimentation velocity of a single particle in the pure-fluid region which, given the parameters considered herein, is equal to $\hat{u}_r = 0.0524$ m/s. We have conducted simulations of this flow with the aforementioned 3D parallel code that we developed. To this end, we employed three different uniform grids consisting of 256, 512 and 1024 points, respectively, in the vertical direction. (Since this is a 1D problem, we used 2 grid points in each of the other directions). In all cases, the time-step is fixed at $\Delta t = 9.38 \times 10^{-7}$ nondimensional units. The final time of the simulation is $t = 1.5$, which is the time that it takes for the sedimentation to be completed. The elapsed time of the simulation with the finest grid on the aforementioned 40-core computer is approximately 96 hours; accordingly the CPU time of the simulation is 96×40 hours.

The evolution of the volume fraction ϕ_s is shown in Figure 1. The images in this Figure show the volume fraction distributions at different times, as computed with the fine grid of 1024 points. Therein we can clearly observe the formation of the three regions mentioned above, namely, dense sediment bed at the bottom, a pure-fluid layer at the top and the granular suspension in between. The whole process is relatively slow due to the high drag that is exerted on the solid particles. At t=1.5 the sedimentation process is nearly completed and almost all solid particles have been accumulated at the bottom sediment bed, above which lies a pure-water column.

The settling velocity of the suspension u_{ss}, i.e. the velocity of the grains inside the homogeneous region with $\phi = 0.1$, is determined by the balance between gravity, buoyancy and interphasial drag. Our simulation predicted that $u_{ss} = 0.56$. Since the top interface necessarily moves at the same velocity, the value of u_{ss} can be calculated on the basis of the position of this interface at different times. Indeed, upon inspection of the interface positions shown in Figure 1 we can directly confirm that $u_{ss} = 0.56$. This result is very close to the value $u_{ss} = 0.59$ obtained from the empirical Richardson-Zaki law [59], $u_{ss} = \hat{u}_{ss}/\hat{u}_r = (1-\phi)^n$ with $n \approx 5$ for small spheres. Also, it is in good agreement with the experimental data for settling velocities of suspensions provided in [60]; see, for example Figure 3 of [60]. Further, it agrees reasonably well with the experimental data of Nicolai et al. [61] according to which $u_{ss} = 0.7 \pm 0.1$

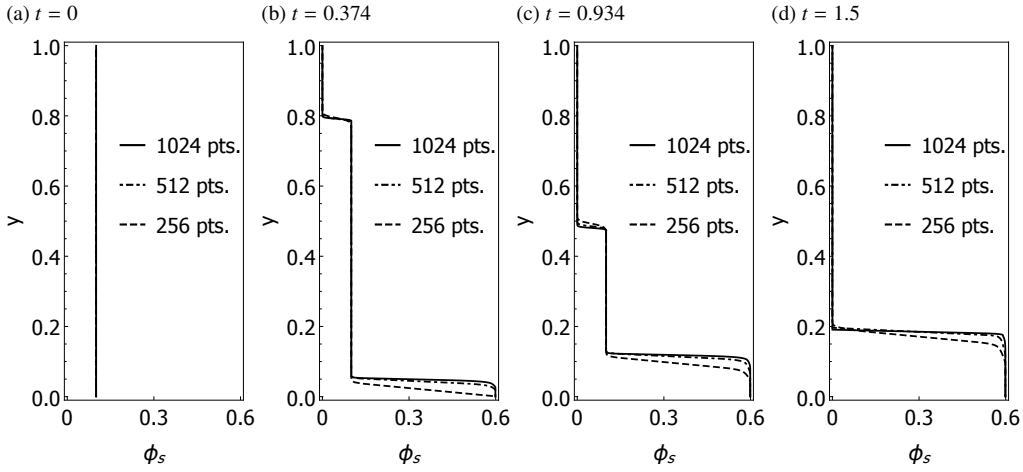

Fig. 2. Sedimentation of a granular suspension: numerical grid-convergence study. The images show plots of the granular volume fractionϕ_s as a function of the wall-normal direction y at different times and computed with 3 different grid sizes. We can observe that the numerically-captured interfaces become sharper as the grid is refined.

for $\phi_s = 0.1$ and spheres of diameter 7.88×10^{-4} m. In the context of our study we performed an additional simulation with initial particle concentration $\phi_s = 0.15$. In this case, our numerical result for the settling velocity is $u_{ss} = 0.43$, which almost coincides with the result of the Richardson-Zaki law $u_{ss} = 0.44$. Also, it is in fairly good agreement with the lower end of the measurements reported in [61], $u_{ss} = 0.57 \pm 0.08$. On the other hand, Balakin et al. [62] reproduced numerically the experiments in [61] and computed $u_{ss} \approx 0.62$ for $\phi_s = 0.15$, which is significantly higher than our result. It should be mentioned however that the flow model in [62] was significantly different from ours. For example, in [62] the pressures of the two phases were set equal, the viscous stresses for the solid phase were modeled as Newtonian and the correlation for the drag coefficient $\hat{\delta}$ was different than the one employed herein.

In order to assess the convergence properties of the algorithm we performed a numerical grid-convergence study for the problem in hand with initial concentration $\phi_s = 0.1$, the results of which are shown in Figure 2. More specifically, the images of this figure show the profiles of ϕ_s along the wall-normal direction y at different times and computed with the 3 different grid sizes mentioned above. In these figures we can readily observe that the numerically-captured interfaces become sharper as the grid is refined. We also infer that the coarser grid (256 points) results in excessive numerical diffusion across the interfaces. Further, we remark that the sediment-fluid interface at the final time of the simulation $t = 1.5$ should be located at $y = 0.166$. Indeed, from Figure 2d we can infer that the numerically captured interface starts at this location but has a finite thickness of 0.02 unit lengths. In any case, the interface-regularization method has been capable of stabilizing the computation of the flow variables across the interfaces for all grid sizes.

At the end of the entire process, the sediment bed should be fully compacted, with ϕ_s being very close to the value of maximum packing $\phi_m = 0.6$. Actually, upon inspection of the compaction equation (21), we can readily infer that ϕ_s can never be exactly equal to ϕ_m because once the intergranular stress becomes very high, then the time derivative of the volume fraction will become negative. In practice however, and given the above expression of the intergranular stress (82), the final value of ϕ_s in the interior of the sediment bed was so close to ϕ_m that its computation would require extremely small and practically unattainable time-steps. For this reason, in this test case we have set a numerical upper bound (cut-off value) of ϕ_s, namely $\phi_s = 0.5999$.

The numerical ramification of the introduction of this cut-off value can be inferred from the velocity and pressure profiles at $t = 1.5$ that are shown in Figure 3a. We see that in the pure-fluid layer ($\phi_s = 10^{-5}$) above the sediment bed, the fluid velocity vanishes and the velocity of the granular phase is equal to unity, i.e. the settling velocity of a single grain. Further, the phasial pressures p_s and p_f are equal, as expected. On the other hand, the volume fraction relaxes at the cut-off value $\phi_s = 0.5999$ everywhere inside the compaction bed. Then, due to the compaction equation (21) we have that, inside the bed, $p_s - p_f = \beta_s$. However, at this cut-off value, β_s is still very small. Consequently, and as evidenced by the pressure plots in Figure 3b, the pressure difference $p_s - p_f$ is also very small and cannot balance out the gravity term in the momentum equation of the granular phase (21). This leads to very small, albeit non-zero,

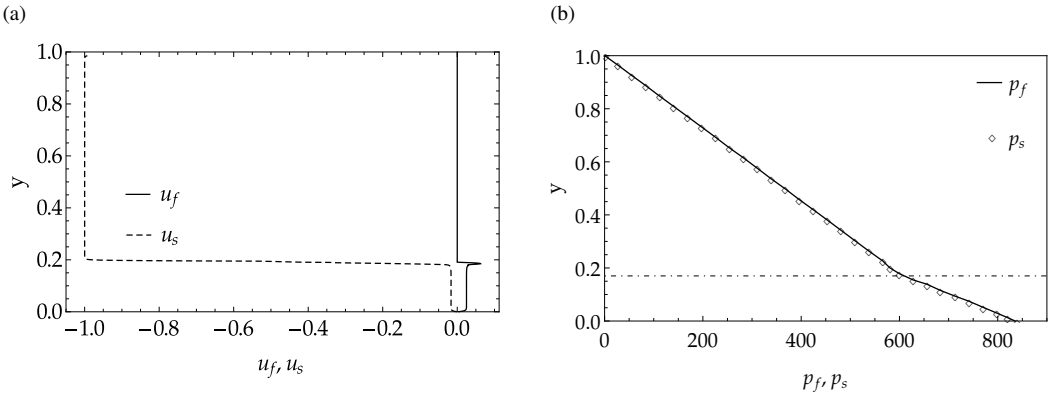

Fig. 3. Sedimentation of a granular suspension. (a) Profiles of the velocities of the two phases near the completion of the sedimentation process, at $t = 1.5$. In the pure-fluid region the fluid velocity is zero and the velocity of the granular phase is equal to the settling velocity of a single grain. Inside the sediment bed, the two velocities assume small but non-zero values of opposite sign, due to the applied numerical cut-off $\phi_s = 0.5999$. (b) Phasial Pressures at $t = 1.5$. In the pure-fluid region the two pressures are equal as expected. On the other hand, inside the sediment bed at the bottom and due to the cut-off in ϕ_s, the pressure-difference is still very small. The horizontal dash-dot line at $y = 0.167$ marks the final position of the bed-fluid interface.

phasial velocities of opposite sign inside the sediment bed.

In other words, due to the applied numerical cut-off of the volume fraction at $\phi_s = 0.5999$, the sediment bed is kept in a state of very slow relaxation. This numerical artifact is a consequence the need to avoid the singularity of the intergranular stress β_s at maximum packing, cf. (82). Although the ramifications of this artifact are rather mild, it is nonetheless instructive to explore ways to eliminate it. An obvious choice would be to select a cut-off value closer to ϕ_m. However, the necessary cut-off value to eliminate this artifact was also too close so ϕ_m and required the use of extremely small time-steps. Given these limitations, we performed simulations of a similar test case but with a modified expression for β_s that we describe below.

4.3. Compaction of a dense bed

In this case we consider the same vertical tube as before (its height is equal to 0.4 m) that contains water and sand. This tube is discretized via a 512-point uniform grid. Initially, a dense sediment bed of $\phi_s = 0.5998$ is located at the bottom third of the tube $0 < y < 0.33$. Above that, the volume fraction decreases monotonically until $y = 0.66$ at which point it is almost equal zero, $\phi_s = 10^{-5}$; see Figure 4. The top third of the tube, $0.66 < y < 1$, is covered by pure water with $\phi_s = 10^{-5}$ as well. All material parameters and boundary conditions are the same as before. In this problem, the granular phase compacts even further due to gravity, thus forming a sediment bed whose concentration is close to maximum packing and a pure-water layer above it. By mass conservation, the final position of the interface between the bed and the pure-water-layer is located at $y = 0.5$.

From a numerical standpoint, we no longer introduce a cut-off value for ϕ_s. Nonetheless, in order to circumvent the problem of excessively small time-steps associated with the use of (82), we employ a slightly modified expression for β_s, namely,

$$\hat{\beta}_s = \begin{cases} -\hat{\beta}_0 \log\left(\frac{\phi_m - \phi_s}{\phi_m}\right), & \text{if} \quad \phi_m - \phi_s \geq \epsilon\,, \\ \hat{\beta}_0 \left(\frac{1}{2}\frac{\epsilon^2}{(\phi_m - \phi_s)^2} - \log(\frac{\epsilon}{\phi_m}) - \frac{1}{2}\right), & \text{if} \quad \phi_m - \phi_s < \epsilon\,, \end{cases} \tag{86}$$

where ϵ is a small parameter. In our study we set $\epsilon = 10^{-2}$, which is equivalent to modifying the original expression (82) for β_s in the interval $0.59 < \phi_s < 0.6$. It is worth noting that even with this expression, the allowable time-steps for stable integration of the governing system are still an order of magnitude smaller than in the previous test case in which we used a cut-off value for ϕ_s.

We simulate the settling and compaction bed for 0.094 time units after which the sediment bed has practically settled to its final position. Overall, this is a slow relaxation process; for example, over 10 time units the volume fraction at the bottom of the tube has evolved merely from $\phi_s = 0.5998$ to $\phi_s \approx 0.59995$. The initial and final profiles of the volume fraction are shown in Figure 4. A close-up of the initial and final volume fraction profiles inside the

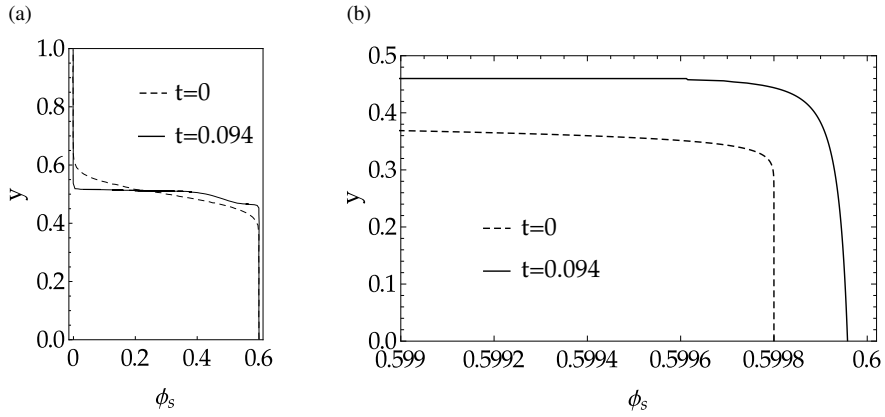

Fig. 4. Compaction of a dense bed. (a) Initial and final volume-fraction distribution across the vertical tube, $t = 0$ and $t = 0.094$, respectively. (b) Close-up of the volume fraction distribution inside the sediment bed.

sediment bed is provided in Figure 4b. In this image we can observe a very small variation of ϕ_s across the bed. In fact, the computed slope of ϕ_s therein coincides with the analytical solution of the governing equations for the corresponding hydrostatics problem. o

The plots of the velocities of the two phases u_s and u_f at different time instances of the compaction process are shown in Figure 5. We can observe that at early times the two phases move to opposite directions. The granular phase settles in the bottom half of the tube due to gravity, thereby displacing the water which moves upward. As in the previous case, the granular velocity u_s in the pure-fluid region equals the reference velocity, i.e. the settling velocity of a single grain in a fluid at rest, $\hat{u}_r = 0.0524$ m/s. At $t = 0.0374$ the compaction process has advanced significantly so that most of the material in the sediment bed is at rest. Finally, at $t = 0.094$ the compaction process is near completion. It is worth noting that the smooth transition zone of u_s from one to zero coincides with the transition of ϕ_s from its maximum value inside the bed to its minimum value $\phi_s = 10^{-5}$ and is due to the slow relaxation above a very dilute suspension above the compacted bed.

In Figure 6 we present plots of phasial pressures p_s and p_f at an early time ($t = 1.87 \times 10^{-4}$) and at the end of the simulations ($t = 0.094$). We can see that at the early stages of the process, the pressure difference $p_s - p_f$ inside the bed is very small. This is mainly due to the small value of β_s at the initial concentration $\phi_s = 0.5998$. At the end of the simulation, however, the volume fraction has increased to $\phi_s \approx 0.59995$, which results to a much higher value of β_s and, in turn, a substantial difference between the two phasial pressures. Further, we see that at the final stages of the process, the momentum equations of the two phases have essentially been reduced to the balance of forces for hydrostatics of granular mixtures, i.e. when both phases are at rest [63, 64]. Moreover, in the interior of the compacted bed the volume-fraction variations are exceedingly small so that both phasial pressures are practically balanced out by buoyancy.

Finally, we present results from a grid-convergence study that we conducted for this test case in order to examine the scaling of the numerical errors of the algorithm. More precisely, we calculate the L_2 norm of the error of the numerical solution at $t = 0.0374$ with respect to a reference solution. Herein, the reference is the numerical solution obtained with the fine grid of 1024 points. For example, the numerical error for the volume fraction is $\mathrm{Err}(\phi_s) = \frac{||\phi_s - \phi_{ref}||_2}{||\phi_{ref}||_2}$, with ϕ_{ref} standing for the reference solution.

In Figure 7 we show the plots of the errors for the volume fraction, granular velocity and pressure difference p_d. We observe that the errors in ϕ_s and u_s decrease monotonically with grid refinement. Further, the numerical solution of both of these quantities convergence to the reference one at a quadratic rate. On the other hand, as regards p_d, we see that it does not convergence to the reference solution monotonically; for example the numerical error with a grid of $n = 256$ points is higher than with a grid of $n = 128$ points. According to these results, a sufficiently refined grid (consisting of at least 512 points) is required in order to achieve satisfactory accuracy. The slow convergence of the numerical prediction of p_d is directly associated to the coupling between the momentum equation for granular phase and the compaction equation that was discussed above and highlights the inherent difficulties in algorithm design for granular suspensions.

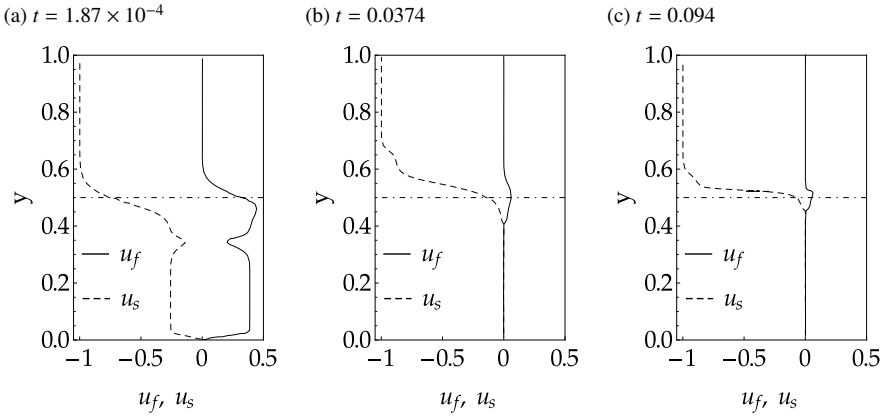

Fig. 5. Compaction of a dense bed: profiles of the phasial velocities u_s and u_f at different times during the compaction process. (a) $t = 1.87 \times 10^{-4}$. At early times there is significant motion of grains downward while the fluid moves in the opposite direction. (b) $t = 0.0374$. The granular phase has almost settled inside the bed, except for a thin region close to the interface. (c) $t = 0.094$. The compaction process is near completion. The horizontal dash-dot line at $y = 0.5$ shows the final location of the interface between the sediment bed and the pure-fluid column.

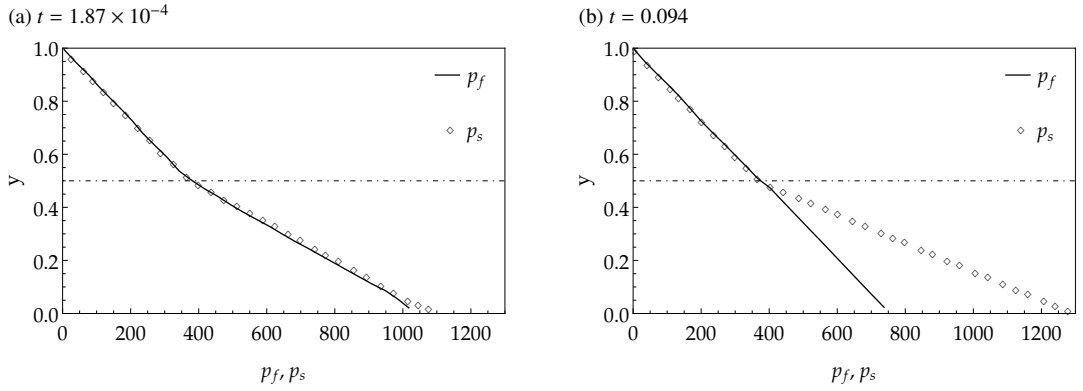

Fig. 6. Compaction of a dense bed: profiles of the phasial pressures profiles at an early stage and at the end of the simulation. (a) $t = 1.87 \times 10^{-4}$, (b) $t = 0.094$. The horizontal dash-dot line at $y = 0.5$ shows the final location of the interface between the sediment bed and the pure-fluid column.

4.4. Collapse of a submerged granular column

Next, we study numerically the collapse of a 2D dense granular column submerged in water. This case is particularly challenging from the numerical perspective because of the development of large velocity variations and the emergence of complex flow structures [16, 65–67]. Additionally, the suspension that is formed after the collapse is dense in some regions but dilute in some others, which implies large variations of the transport coefficients and parameters of the granular phase. Due to these challenges, this case is an important benchmark for flow models and associated numerical methods of granular suspensions.

The flow domain is a rectangle, with a length of 1.8 m and a height of 0.3 m. The granular column is also a rectangle; its length is 0.09 m and its height is 0.18 m. The volume fraction inside the column is set $\phi_s = 0.59$. The column is placed next to the left boundary of the computational domain; see Figure 8a. Additionally, we place a dense granular bed on the bottom of the domain, also with $\phi_s = 0.59$, so as to circumvent the complexities of assigning slip boundary conditions for the velocity of the granular phase at a solid wall. The height of this layer is 0.04 m. The remaining part of the domain is filled with water; therein the concentration of the volume fractions is set at $\phi = 10^{-5}$. As regards boundary conditions, the top and bottom boundaries are assumed to be rigid walls, whereas the left boundary is a symmetry plane. At the right boundary we apply outflow (zero-Neumann) conditions.

For non-dimensionalization purposes, the reference length is the height of the domain, $\hat{h} = 0.3$ m, and the reference velocity is $\hat{u}_r = (2\hat{g}\hat{h})^{1/2} = 2.4$ m/s. The computational domain is discretized with a uniform grid consisting of 512×256 points. The simulation is performed with our 3D code but since this is a 2D simulation, we used 2 grid

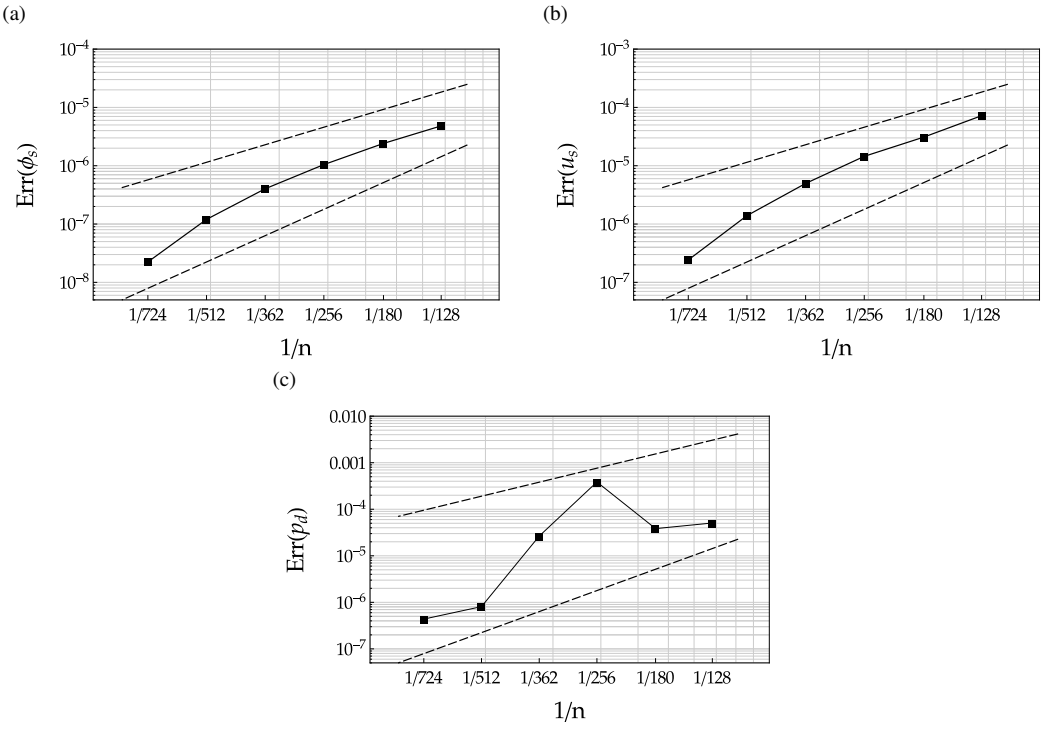

Fig. 7. Compaction of a dense bed: grid-convergence study of the numerical predictions at $t = 0.0374$. L_2 norm of the error in the computation of various flow quantities with respect to a reference solution with 1024 points. (a) ϕ_s, (b) u_s, (c) p_d. The quantity n stands for the number of points of the computational grid. The upper and lower dashed lines correspond to the second- and third-order convergence rates, respectively.

points in the z direction. The time-step for this simulation is $\Delta t = 10^{-4}$ non-dimensional time units. The final time of the simulation is 14 units, which is the time that it takes for the collapse to be completed. The elapsed real time of the simulation is approximately 250 hours. Accordingly, the CPU time with the afore-mentioned 40-core computer is 250×40 hours.

By applying the interface-regularization technique that is described in the Appendix, we have spread the initial column-water interface across 15 computational cells. Also, in order to avoid very small time-steps, the singularity of the intergranular stress β_s at the point of maximum packing, $\phi_m = 0.6$, is circumvented by setting a numerical cut-off for the volume fraction at $\phi_s = 0.5999$.

The evolution of the granular volume fraction at different time instances is shown in Figure 8. In Figure 8a we have plotted the initial configuration of the column, whereas in Figure 8b we present contour plots of ϕ_s at an instance during the early stages of the collapse, $t = 2$. In this plot, we can observe that the material adjacent to the lateral side of the column slides downward, leading to the formation of local instabilities along the granular column - water interface. Further, next to the base of the column, a plume of ejected material rises due to the impact of the fallen granular material with the bottom layer. These flow structures have also been observed in the experiments reported in [65, 66]. Moreover, the evolution of the flow as predicted by our simulation agrees well with the one described in those experimental studies.

In Figure 8c we show contour plots of the volume fraction at an advanced state of the process, $t = 7$. According to this figure, a substantial portion of the granular material has fallen, which reduces the column to a pile of triangular shape. Further, we can observe that the collapsed material does not disperse in the water but, instead, flows close to the bottom granular bed forming a stream that is characterized by high shear and successive spanwise vortices. Finally, in Figure 8d we present contour plots at $t = 14$. At this instance the collapse of the granular column is practically complete. More specifically, the remnant triangular pile has stopped evolving and the fallen material has formed a mobile layer that propagates toward the right outflow boundary of the domain. Some parts of this layer are quite dense, with ϕ_s reaching and even exceeding 0.4.

According to our simulations, the remnant triangular pile has a slope of approximately 35°. This prediction

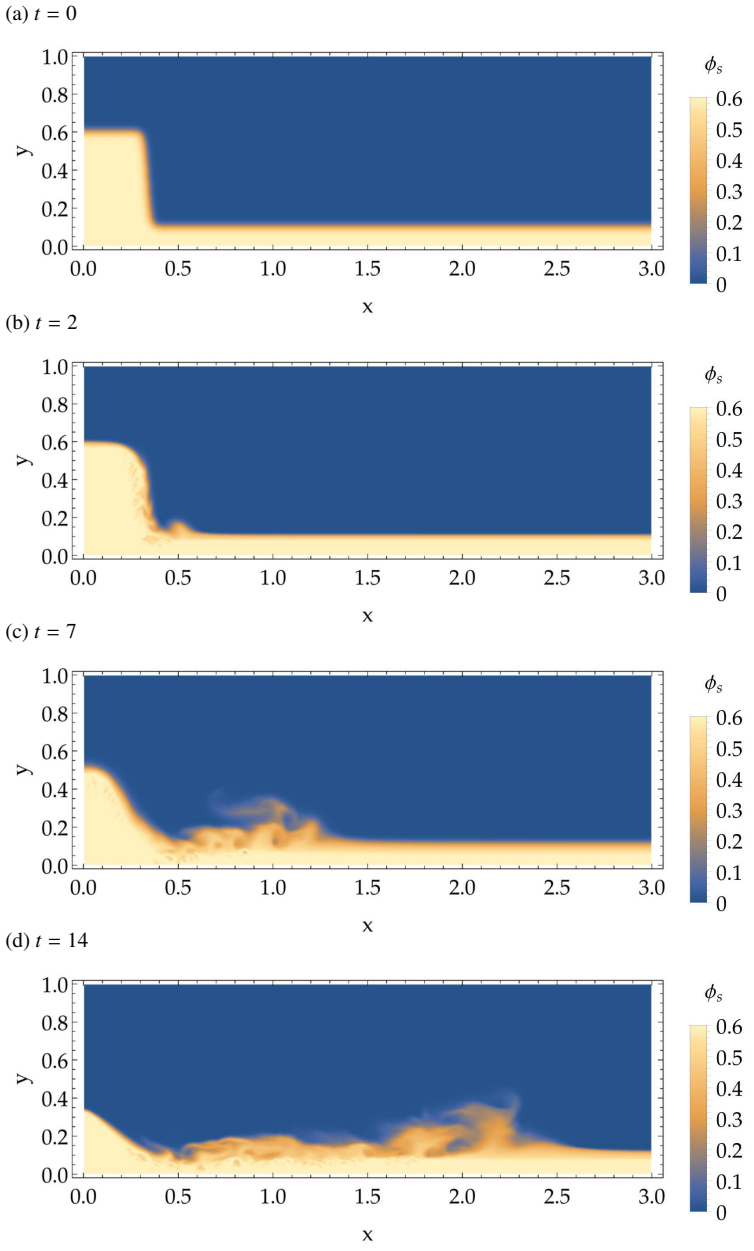

Fig. 8. Collapse of a granular column submerged in water: contour plots of the volume fraction at different instances. (a) $t = 0$**. (b)** $t = 2$**. (c)** $t = 7$**. (d)** $t = 14$**. At the early stages the side of the column slides due to gravity. Subsequently the column reduces to a triangular pile while the collapsed material is being washed away.**

compares well with the values reported in [65]. More specifically, the authors of [65] reported values of the apex angle that are scattered around 32° reported in [65] for granular columns of aspect ratios lower than 5 (in our study the aspect ratio of the column is 2). This can also been evidenced In Figure 9 which shows contours for the granular volume fraction at the end of our simulation, $t = 14$ and a superposed line of 32° slope at the side of the triangular pile. Our computations predict that the height of the remnant pile is equal to 65% of the initial height of the column. However, in the experiments reported in [65], the height of the pile is larger and equal to 74% of the height of the column. A possible explanation for this difference is that the height of the pile is very sensitive with respect to the initial volume fraction of the granular column, which has been documented in the experimental studies [66, 67].

Additional numerical testing that we conducted within the framework of our study confirmed this finding. More

specifically, we performed simulations with different initial volume fractions and observed that no pile is formed if initially ϕ_s is less than 0.55, in which cases the column collapses entirely (i.e. without leaving a remnant pile) and all of its material is washed away. This type of collapse can be traced to the fact that the granular viscous forces are very stiff with respect to the volume fraction. Therefore, at lower ϕ_s the granular material falls fast. Further, as discussed above, compaction is a slow process so that the material that in the core of the column does not compact fast enough to increase its viscosity. As a result, the grains keep falling sideways until the entire column is collapsed [67].

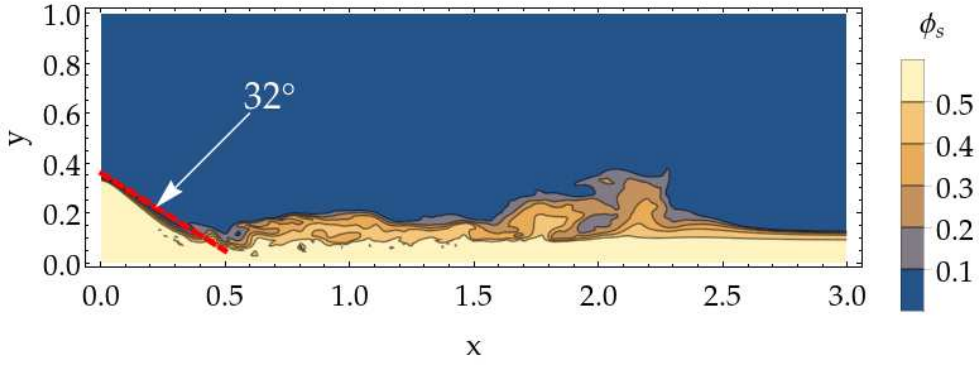

Fig. 9. Collapse of a granular column submerged in water: contours of the granular volume fraction $t = 14$ for $\phi_s = 0.1, 0.2, 0.3, 0.4$, and 0.5. The inclination of the red dashed line is 32° and corresponds to the experimental data of [65] for the remnant pile after the collapse.

Next, we present results for the velocity fields. In Figure 10 we show contour plots of the vertical velocity components for both phases (u_{s_y} and u_{f_y}) at $t = 2$. From these plots we can confirm that the collapse is driven by the sliding motion of the material adjacent to the lateral side of the column. Since the column is quite dense, the interphasial drag coefficient is high and, therefore, the velocities of the two phases become equal in a short time. The vertical component of the granular velocity u_{s_y} at later times ($t = 7$ and $t = 14$) is shown in Figure 11. At $t = 7$, the remnant pile is already formed but, as can be inferred from the velocity plots in Figure 11a, the material at its lateral side is still mobile, which implies that the collapse is still under way. Further, in this Figure we can observe strong variations of the velocity on the surface of the pile. These variations signify spanwise vortices that are formed as the fallen material is convected away from the pile. At $t = 14$ the collapse is almost complete and the magnitude of the velocity is significantly reduced, as can be observed in Figure 11b. According to this figure, only a very thin region is still mobile at the surface of the pile and the remaining collapsed material is convected away and toward the exit boundary of the domain.

The plots of the streamwise velocity components, shown in Figure 12, further confirm that once the column collapse is completed, the fallen material forms a dense mobile layer. Inside this layer, the velocity amplitude of the particulate phase remains high even at large distances from the location of the column. Moreover, the fluid velocity is also high and comparable to the one of the particulate phase. This is because the mobile layer is quite dense, which translates to high interphasial drag coefficient.

Finally, it is worth mentioning an interesting detail regarding the interaction between the fallen material and the thin granular bed that sits on top of the bottom boundary. During the collapse, the bed in proximity of the column becomes mobilised as the collapsing material falls on it. This can be readily inferred from Figure 13 which shows vector plots of the granular velocity and contour plots of its amplitude at $t = 7$ and $t = 14$. The increased velocities below the initial height of the bed also imply that the thin bed becomes subject to scouring. In fact, some material that was initially in the bed is entrained in the dense mobile layer that moves away from the column.

5. Conclusions

In this paper we presented an algorithm for the time-accurate calculation of two-phase flows of granular suspensions. These mixtures are immiscible and, therefore, the velocities of the two phases are non-solenoidal even for constant material densities. Accordingly, the granular phase can compact, expand and dilate. Also, granular suspensions are characterized by a complex rheological behaviour.

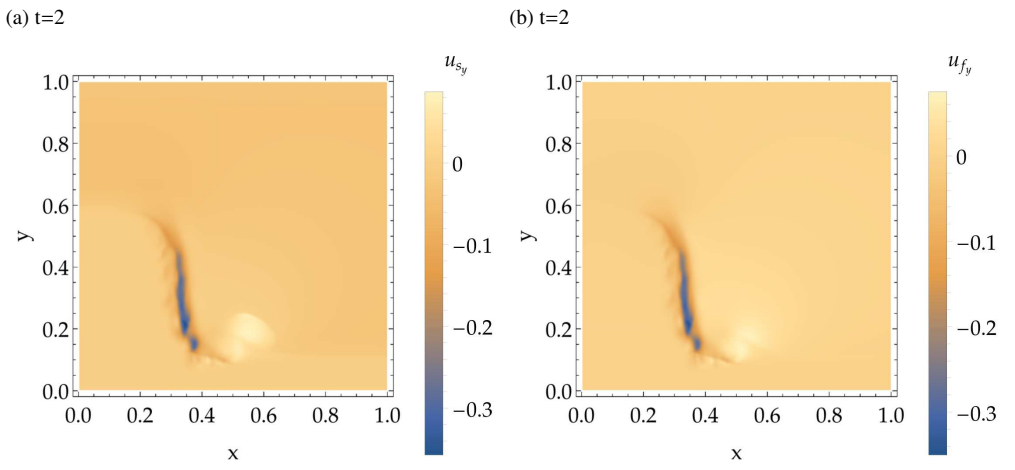

Fig. 10. Collapse of a granular column submerged in water: contour plots of the vertical velocity components of the two phases (u_{s_y} and u_{f_y} at $t = 2$. (a) granular velocity component u_{s_y}. (b) fluid velocity component u_{f_y}. These plots confirm that the column collapse is driven by the sliding motion of the material adjacent to the lateral side of the column. The velocities of the two phases are comparable due to high interphasial drag coefficient.

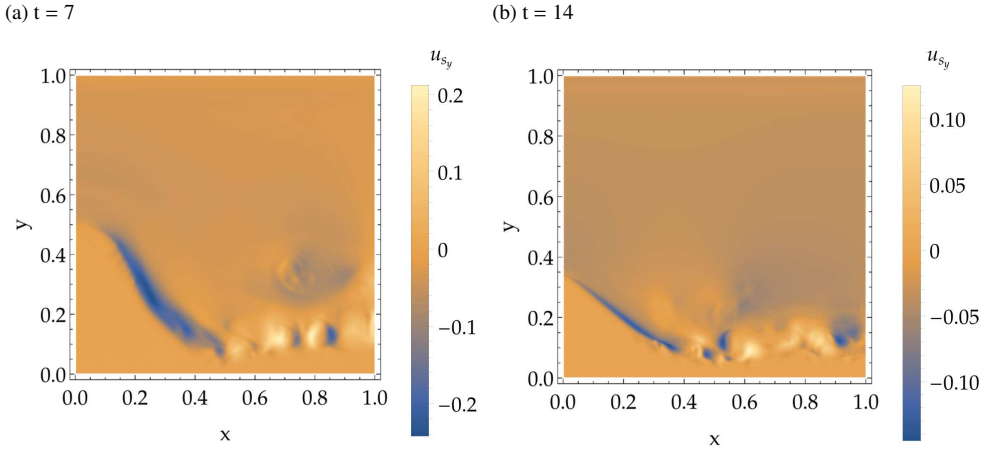

Fig. 11. Collapse of a granular column submerged in water: contour plots of the vertical component of the granular velocity u_{s_y}. (a) $t = 7$. (b) $t = 14$.

The proposed algorithm is based on a two-stage predictor-corrector method for advancing the solution in time. The computation of the phasial pressures is achieved via a generalization of the standard Chorin-Temam projection method for non-solenoidal fields that reduces two second-order elliptic equations. The implementation of this method addresses in an efficient manner the strong coupling between the momentum balance laws and the governing equation for the granular volume fraction which, as shown herein, can play a destabilizing role in the computations. Spatial discretization is performed on a collocated grid. In order to avoid the well known odd-even decoupling problem associated with these grids we have implemented a suitable flux- interpolation technique for the convective fluxes of the governing equations.

This algorithm is useful for the simulation of flows of dense suspensions, flows with high volume-fraction variations or material interfaces, as well as for unsteady fluidsolid interaction problems. Its performance has been assessed via a series of test cases, such as sedimentation of a suspension and the collapse of a submerged granular column and via additional numerical-convergence studies.

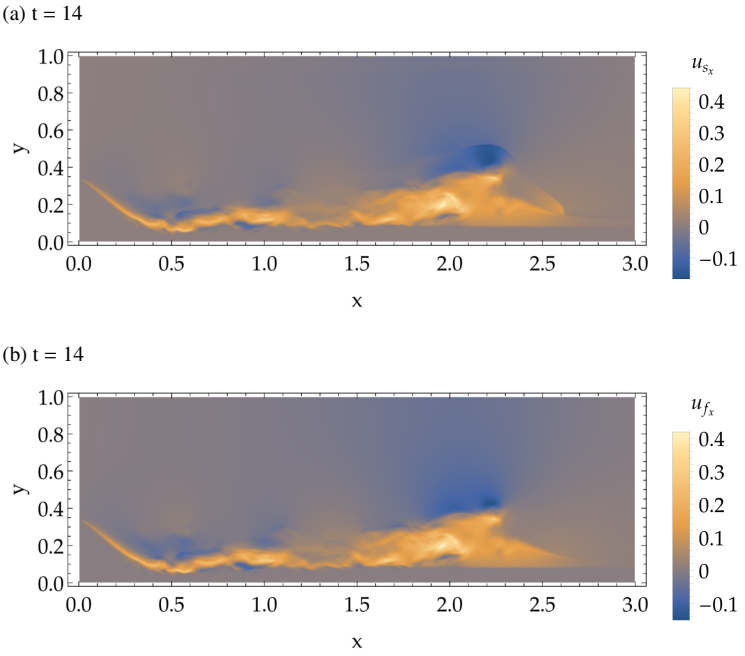

Fig. 12. Collapse of a granular column submerged in water: contour plots of the horizontal velocity components of the two phases (u_{s_x} and u_{f_x}) at $t = 14$. (a) granular velocity component u_{s_x}. (b) fluid velocity component u_{f_x}. The remaining collapsed material has formed a mobile layer that is washed away.

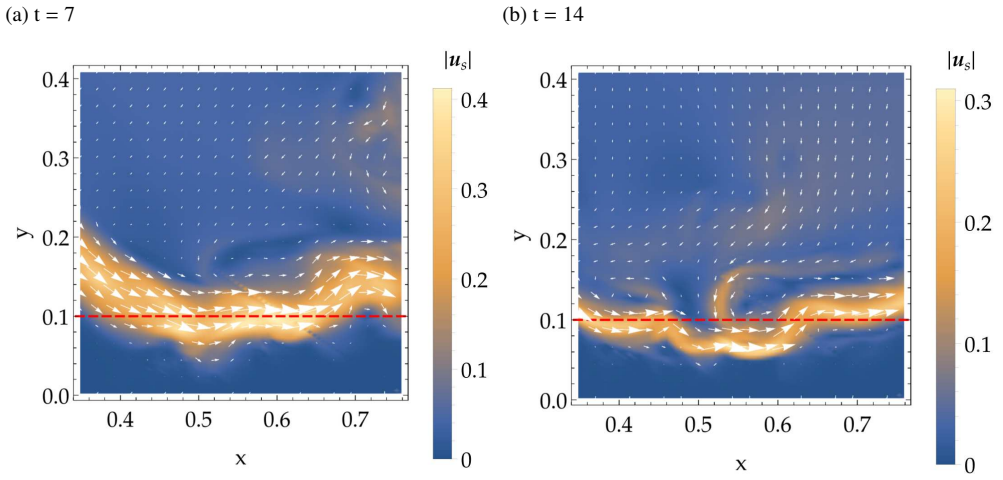

Fig. 13. Collapse of a granular column submerged in water: vector plots of the granular velocity u_s and contour plots of its amplitude at the right of the column. (a) $t = 7$. (b) $t = 14$. The bed in proximity of the column becomes mobilised as the collapsing material falls on it and becomes subject to scouring.

Acknowledgments

Financial support has been provided by the European Commission via SEDITRANS (REA grant agreement no. 607394), an ITN project of the Marie Curie Actions of the 7th Framework Programme.

Appendix: Auxiliary fluxes for the convective terms and interface-regularization scheme

For the description of the flux-interpolation technique we assume, for the sake of simplicity, that the computational domain is a rectangular parallelepiped discretized by a uniform mesh. In particular, the mesh consists of a finite collection of equidistant 3-dimensional rectangles K_{ijk}, $i = 1, ...M_x$, $j = 1, ..., M_y$, $k = 1, ..., M_z$, lexicographically ordered with respect to the Cartesian coordinates of their cell centers (x_i, y_j, z_k). The length of the cells in each dimension is denoted by Δx, Δy and Δz, respectively. Throughout this appendix, the following standard notation convention is adopted for a generic quantity f,

$$f(i, j, k) \; = f(x_i, y_j, z_k)\,, \tag{87}$$

$$f(i + \tfrac{1}{2}, j + \tfrac{1}{2}, k + \tfrac{1}{2}) \; = f(x_i + \tfrac{\Delta x}{2}, y_j + \tfrac{\Delta y}{2}, z_k + \tfrac{\Delta z}{2})\,. \tag{88}$$

urther, it is well suited for the di- rect numerical simulation of unsteady fluidsolid interaction Further, two discrete operators are introduced. First, the finite-difference operator acting on a function $f(x_i, y_j, z_k)$. When applied to the x-direction, this operator is given by

$$\frac{\delta f(i, j, k)}{\delta x} \;=\; \frac{f(x_i + \frac{\Delta x}{2}, y_j, z_k) - f(x_i - \frac{\Delta x}{2}, y_j, z_k)}{\Delta x}\,. \tag{89}$$

Second, the linear interpolation operator is introduced. Along the x-direction its expression is given by

$$\overline{f}^{x}(i, j, k) \; = \frac{f(x_i + \frac{\Delta x}{2}, y_j, z_k) + f(x_i - \frac{\Delta x}{2}, y_j, z_k)}{2}\,. \tag{90}$$

Expressions for the above operators acting on the other directions can be directly obtained in an analogous manner.

In order to compute the convective fluxes at the cell interfaces, we observe that an interpolation scheme can be deduced from the discretized momentum equations for the two phases, (48) and (55) when applied at cell interfaces. For the sake of brevity, we provide below the resulting relations for an interface normal to the (x_2, x_3) plane; expressions for all the other cell interfaces can be obtained by permutation of index (i, j, k) and of sign $(+\frac{1}{2}, -\frac{1}{2})$. Also for the sake of brevity, the expressions do not explicitly indicate the time discretization, so that they are valid at any time instant; the only exceptions are the provisional velocities $\tilde{u}_{s_x}$ and $\tilde{u}_{f_x}$, for which the notation corresponds to the predictor stage; in the corrector stage the updated values $\check{u}_{s_x}$ and $\check{u}_{f_x}$ should be used instead.

The spatial discretization of (48) and (55) at a cell interface reads

$$\begin{aligned}\phi_s(i + \tfrac{1}{2}, j, k)\, u_{s_x}(i + \tfrac{1}{2}, j, k) \; &= \phi_s(i + \tfrac{1}{2}, j, k)\, \tilde{u}_{s_x}(i + \tfrac{1}{2}, j, k) \\ &\quad - \frac{\Delta t}{\rho_s} \frac{\delta p_d(i + \frac{1}{2}, j, k)}{\delta x} \; + \Delta t \frac{\rho_s - \rho_f}{\rho_s} \phi_s(i + \tfrac{1}{2}, j, k)\, \boldsymbol{e}_x \cdot \boldsymbol{g}\,,\end{aligned} \tag{91}$$

and

(92)

$$\begin{aligned}\phi_f(i + \tfrac{1}{2}, j, k)\, u_{f_x}(i + \tfrac{1}{2}, j, k) \; &= \phi_f(i + \tfrac{1}{2}, j, k)\, \tilde{u}_{f_x}(i + \tfrac{1}{2}, j, k) \\ &\quad - \frac{\Delta t}{\rho_f} \phi_f(i + \tfrac{1}{2}, j, k) \frac{\delta p'_f}{\delta x}(i + \tfrac{1}{2}, j, k)\,,\end{aligned} \tag{93}$$

respectively

The quantities at the right-hand sides of the above equations can be approximated as follows,

$$\phi_s(i + \tfrac{1}{2}, j, k)\, \tilde{u}_{s_x}(i + \tfrac{1}{2}, j, k) \; \approx \overline{\phi_s(i + \tfrac{1}{2}, j, k)\, \tilde{u}_{s_x}(i + \tfrac{1}{2}, j, k)}^{x}\,, \tag{94}$$

$$\phi_f(i + \tfrac{1}{2}, j, k)\, \tilde{u}_{f_x}(i + \tfrac{1}{2}, j, k) \; \approx \overline{\phi_f(i + \tfrac{1}{2}, j, k)\, \tilde{u}_{f_x}(i + \tfrac{1}{2}, j, k)}^{x}\,, \tag{95}$$

$$\phi_s(i + \tfrac{1}{2}, j, k)\, \boldsymbol{e}_x \cdot \boldsymbol{g} \; \approx \overline{\phi_s(i + \tfrac{1}{2}, j, k)}^{x}\, \boldsymbol{e}_x \cdot \boldsymbol{g}\,. \tag{96}$$

Next, the following short-hand notation is introduced,

$$M_s^x(i+\tfrac{1}{2},j,k) \;= \overline{\phi_s(i+\tfrac{1}{2},j,k)\,\tilde{u}_{s_x}(i+\tfrac{1}{2},j,k)}^{\,x} - \frac{\Delta t}{\rho_s}\frac{\delta p_d(i+\tfrac{1}{2},j,k)}{\delta x} + \Delta t\frac{\rho_s-\rho_f}{\rho_s}\overline{\phi_s(i+\tfrac{1}{2},j,k)}^{\,x}\boldsymbol{e}_x\cdot\boldsymbol{g}\,, \tag{97}$$

and

$$M_f^x(i,j,k) \;= \overline{\phi_f(i+\tfrac{1}{2},j,k)\,\tilde{u}_{f_x}(i+\tfrac{1}{2},j,k)}^{\,x} - \frac{\Delta t}{\rho_f}\overline{\phi_f(i+\tfrac{1}{2},j,k)}^{\,x}\;\frac{\delta p_f'(i+\tfrac{1}{2},j,k)}{\delta x}\,. \tag{98}$$

The quantities $M_\alpha^x(i-\frac{1}{2},j,k)$, $\alpha=s,f$ are obtained directly by replacing $i+\frac{1}{2}$ by $i-\frac{1}{2}$ in the above expressions, and the quantities M_α^y and M_α^z are defined by direct analogy.

Relations (97) and (98) can be used to discretize the convective fluxes. To this end, we apply the divergence theorem on an arbitrary cell K_{ijk},

$$\int_{K_{ijk}}\nabla\cdot(\phi_\alpha\boldsymbol{u}_\alpha\otimes\boldsymbol{u}_\alpha)\mathrm{d}\mathbf{x} \;=\; \int_{\partial K_{ijk}}\phi_\alpha\boldsymbol{u}_\alpha\otimes\boldsymbol{u}_\alpha\cdot\,\mathrm{d}\mathbf{S}\,,\quad \alpha=s,f\,. \tag{99}$$

Then, by discretizing the right-hand side of (99) via equations (97) – (98), we obtain the following approximations for the convective fluxes,

$$\begin{aligned}\int_{\partial K_{ijk}}\phi_\alpha\boldsymbol{u}_\alpha\otimes\boldsymbol{u}_\alpha\cdot\,\mathrm{d}\mathbf{S} \;\approx\; &\frac{M_\alpha^x(i+\frac{1}{2},j,k)\overline{\boldsymbol{u}}_{\alpha_l}^x - M_\alpha^x(i-\frac{1}{2},j,k)\overline{\boldsymbol{u}}_{\alpha_l}^x}{\Delta x}+\\ &\frac{M_\alpha^y(i,j+\frac{1}{2},k)\overline{\boldsymbol{u}}_{\alpha_l}^y - M_\alpha^y(i,j-\frac{1}{2},k)\overline{\boldsymbol{u}}_{\alpha_l}^y}{\Delta y}+\\ &\frac{M_\alpha^z(i,j,k+\frac{1}{2})\overline{\boldsymbol{u}}_{\alpha_l}^z - M_\alpha^z(i,j,k-\frac{1}{2})\overline{\boldsymbol{u}}_{\alpha_l}^z}{\Delta z}\,,\quad \alpha=s,f\,.\end{aligned} \tag{100}$$

With regard to the interface-regularization scheme, as mentioned above, the basic idea is to replace the values of ϕ_s in the vicinity of steep gradients by the values of a smoother, and preferably compactly supported. This can be achieved via a simple parabolic regularization that consists of the following steps.

1) For every computational cell K_{ijk}, we compare the value of ϕ_s^{n+1} at this cell with the ones at the neighboring cells K'. The volume fraction at the cell K_{ijk} is flagged for regularization when

$$|\phi_s^{n+1}(K_{ijk})-\phi_s^{n+1}(K')|>\delta_1\,,$$

for a positive constant $\delta_1>0$.

2) The regularized values ϕ_s^r are computed by iterating the following parabolic problem,

$$\frac{\phi_s^{r+1}-\phi_s^r}{\Delta t} \;=\epsilon\,\nabla^2\phi_s^r\,, \tag{101}$$

$$\phi_s^0 \;=\phi_s^{n+1}\,, \tag{102}$$

where ϵ is a suitably chosen regularization parameter. The iteration is terminated once the following condition is met,

$$|\phi_s^{r+1}(K_{ijk})-\phi_s^{r+1}(K')| \;\le\; \delta_2\,,\quad \forall K_{ijk}\,, \tag{103}$$

with $\delta_2\le\delta_1$. If $\delta_2=\delta_1$ the regularization procedure can potentially be performed at every time iteration; by choosing a lower δ_2, the amount of artificial diffusion can be controlled depending on the specific problem.

3) The regularized values ϕ_s^{r+1} are used as updated values of the volume fraction.

References

[1] J. Duran, Sands, Powders, and Grains: An Introduction to the Physics of Granular Materials, Springer, 2000.
[2] P. Richard, M. Nicodemi, R. Delannay, P. R. D. Bideau, Slow relaxation and compaction of granular systems, Nat. Mater. 4 (2005) 121–128.
[3] H. Jaeger, S. Nagel, Physics of the Granular State, Science 255 (1992) 1523–1531.
[4] T. Homan, C. Gjaltema, D. van der Meer, Collapsing granular beds: The role of interstitial air, Phys. Rev. E 89 (2014) 052204.
[5] W. Russel, Review of the Role of Colloidal Forces in the Rheology of Suspensions, J. Rheol. 24 (1980) 287–317.
[6] J. Stickel, R. Powell, Fluid mechanics and rheology of dense suspensions, Annu. Rev. Fluid Mech. 37 (2005) 129–149.
[7] R. Phillips, R. Armstrong, R. Brown, A. Graham, J. Abbott, A constitutive equation for concentrated suspensions that accounts for shear-induced particle migration, Phys. Fluids A 4 (1991) 30–40.
[8] J. Morris, F. Boulay, Curvilinear flows of noncolloidal suspensions: The role of normal stresses, J. Rheol. 43 (1999) 1213–1237.
[9] G. MiDi, On dense granular flow, Eur. Phys. J. E 14 (2004) 341–365.
[10] P. Jop, Y. Forterre, O. Pouliquen, A constitutive law for dense granular flows, Nature 441 (2006) 727–730.
[11] J. Stickel, R. Phillips, R. Powell, A constitutive model for microstructure and total stress in particulate suspensions, J. Rheol. 50 (2006) 379–413.
[12] D. Monsorno, C. Varsakelis, M. Papalexandris, A thermomechanical model for granular suspensions, J. Fluid Mech. 808 (2016) 410–440.
[13] M. Denn, J. Morris, Rheology of non-brownian suspensions, Annu. Rev. Chem. Biomol. Eng. 5 (2014) 203–228.
[14] K. Yapici, R. L. Powell, R. J. Phillips, Particle migration and suspension structure in steady and oscillatory plane Poiseuille flow, Phys. Fluids 21 (2009) 053302.
[15] L. Ouriemi, P. Aussillous, E. Guazzelli, Sediment dynamics. Part 1. Bed–load transport by laminar shearing flows, J. Fluid Mech. 636 (2009) 295–319.
[16] P.-Y. Lagrée, L. Staron, S. Popinet, The granular column collapse as a continuum: validity of a two-dimensional Navier–Stokes model with a $\mu(I)$–rheology, J. Fluid Mech. 686 (2011) 378–408.
[17] C. Varsakelis, M. Papalexandris, A numerical method for two-phase flows of dense granular mixtures, J. Comput. Phys. 257 (2014) 737–756.
[18] C. Varsakelis, D. Monsorno, M. Papalexandris, Projection methods for two velocity-two pressure models for flows of heterogeneous mixtures, Comput. Math. Appl. 70 (2015) 1024–1045.
[19] D. Monsorno, C. Varsakelis, M. Papalexandris, Poiseuille flow of dense non-colloidal suspensions: the role of intergranular and nonlocal stresses in particle migration, J. Non-Newton. Fluid 247 (2017) 229–238.
[20] P. Nott, J. Brady, Pressure-driven flow of suspensions: simulation and theory, J. Fluid Mech. 275 (1994) 157–199.
[21] M. Goodman, S. Cowin, A Continuum Theory for Granular Materials, Arch. Rat. Mech. Anal. 44 (1972) 249–266.
[22] M. Papalexandris, A two-phase model for compressible granular flows based on the theory of irreversible processes, J. Fluid Mech. 517 (2004) 103–112.
[23] C. Varsakelis, M. Papalexandris, Low-Mach-number asymptotics for two-phase flows of granular materials, J. Fluid Mech. 669 (2011) 472–497.
[24] C. Varsakelis, M. Papalexandris, On the relevance of Low-Mach-number Asymptotics in Thermodynamics of Heterogeneous, Immiscible Mixtures, J. Non-equil. Thermody. 42 (2017) 99–112.
[25] M. Baer, J. Nunziato, A two-phase mixture theory for the deflagration-to-detonation transition (DDT) in reactive granular materials, Int. J. Multiphas. Flow 12 (1986) 861–889.
[26] J. Bdzil, R. Menikoff, S. Son, A. Kapila, D. Stewart, Two-phase modelling of deflagration-to-detonation transition in granular materials: A critical examination of modelling issues, Phys. Fluids 11 (1999) 378–492.
[27] C. Josserand, P.-Y. Lagrée, D. Lhuillier, Stationary shear flows of dense granular materials: A tentative continuum modelling, Eur. Phys. J. E 14 (2004) 127–135.
[28] C. Josserand, P.-Y. Lagrée, D. Lhuillier, Granular pressure and the thickness of a layer jamming on a rough incline, Europhys. Lett. 73 (2005) 363.
[29] A. Chorin, A numerical method for solving incompressible viscous flow problems, J. Comput. Phys. 2 (1967) 12–26.
[30] R. Temam, Une méthode d'approximation des solutions des équations de Navier-Stokes, Bull. Soc. Math. France 98 (1968) 115–152.
[31] F. Nicoud, Conservative high-order finite-difference schemes for low-Mach number flows, J. Comput. Phys. 158 (2000) 71–97.
[32] B. Lessani, M. Papalexandris, Time-accurate calculation of variable density flows with strong temperature gradients and combustion, J. Comput. Phys. 212 (2006) 218–246.
[33] P. Antoniadis, M. Papalexandris, Dynamics of shear layers at the interface of a highly porous medium and a pure fluid, Phys. Fluids 27 (2015) 014104.
[34] M. Papalexandris, P. Antoniadis, A thermo-mechanical model for flows in superposed porous and fluid layers with interphasial heat and mass exchange, Int. J. Heat Mass Tran. 88 (2015) 42–54.
[35] C. Varsakelis, M. Papalexandris, Numerical simulation of subaqueous chute flows of granular materials, Eur. Phys. J. E 38 (2015) 40.
[36] A. Cook, J. Riley, Direct numerical simulation of a turbulent reactive plume on a parallel computer, J. Comput. Phys. 129 (1996) 263–283.
[37] J. Kim, P. Moin, Application of a fractional step method to incompressible Navier–Stokes equations, J. Comput. Phys. 59 (1985) 308–323.
[38] B. Lessani, M. Papalexandris, Numerical study of turbulent channel flow with strong temperature gradients, Int. J. Numer. Meth. Heat Fluid Flow 18 (2008) 545–556.
[39] D. Brown, R. Cortez, M. Minion, Accurate projection methods for the incompressible Navier–Stokes equations, J. Comput. Phys. 168 (2001) 464 – 499.
[40] C. Rhie, W. Chow, Numerical study of the turbulent flow past an airfoil with trailing edge separation, AIAA J. 21 (1983) 1525–1532.
[41] T. S. M.M. Rahman, A. Miettinen, Modified simple formulation on a collocated grid with an assessment of the simplified quick scheme, Numer. Heat Transf. Part B, Fundam. 30 (1996) 291–314.
[42] S.-K. Choi, S.-O. Kim, C.-H. Kim, H.-K. Choi, Use of momentum interpolation method for flows with a large body force, Numer. Heat Transf. Part B, Fundam. 43 (2003) 267–287.
[43] J. Mencinger, I. Zûn, On the finite volume dicretization of discontinuous body force field on collocated grids: Application to VOF method, J. Comput. Phys. 221 (2007) 524–538.

[44] S. Zhang, X. Zhao, S. Bayyuk, Generalized formulations for the Rhie–Chow interpolation, J. Comput. Physics 258 (2014) 880 – 914.
[45] P. Colella, Multidimensional upwind methods for hyperbolic conservation laws, J. Comput. Phys. 87 (1990) 171–200.
[46] G. Grün, On convergent schemes for diffuse interface models for two–phase flow of incompressible fluids with general mass densities, SIAM J. Numer. Anal. 51 (2013) 3036–3061.
[47] H. Abels, L. Diening, Y. Terasawa, Existence of weak solutions for a diffuse interface model of non–Newtonian two-phase flows, Nonlinear0 Anal. Real World Appl. 15 (2014) 149 – 157.
[48] D. Monsorno, Modelling and simulation of fluid-saturated granular materials with application to sedimentation flows, PhD Thesis, Université catholique de Louvain, 2018.
[49] S. Balay, et al., PETSc Web page, 2018. URL: `http://www.mcs.anl.gov/petsc`.
[50] S. Benyahia, M. Syamlal, T. O'Brien, Extension of Hill-Koch-Ladd drag correlation over all ranges of Reynolds number and solids volume fraction, Powder Technol. 162 (2005) 166–174.
[51] S. Passman, J. Nunziato, P. Bailey, K. Reed, Shearing motion of a fluid-saturated granular material, J. Rheol. 20 (1986) 167–192.
[52] W. Elban, M. Chiarito, Quasi-static compaction study of coarse HMX explosive, Powd. Techn. 46 (1986) 181–193.
[53] J. Powers, D. Stewart, H. Krier, Analysis of steady compaction waves in porous materials, J. Appl. Mech. 59 (1989) 15–24.
[54] K. Yeo, M. Maxey, Numerical simulations of concentrated suspensions of monodisperse particles in a poiseuille flow, J. Fluid Mech. 682 (2011) 491–518.
[55] C. Varsakelis, M. Papalexandris, Stability analysis of Couette flows of spatially inhomogeneous complex fluids, Proc. R. Soc. A 471 (2015) 20150529.
[56] C. Varsakelis, M. V. Papalexandris, Stability of wall bounded, shear flows of dense granular materials: the role of the Couette gap, the wall velocity and the initial concentration, J. Fluid Mech. 791 (2016) 384–413.
[57] M. Holems, N. Parker, M. Povey, Temperature dependence of bulk viscosity in water using acoustic spectroscopy, J. Phys.: Conf. Ser. 269 (2011) 012011.
[58] J. Brady, A. Khair, M. Swaroop, On the bulk viscosity of suspensions, J. Fluid Mech. 554 (2006) 109–123.
[59] J. Richardson, W. Zaki, Sedimentation and fluidization: Part I, Trans. Inst. Chem. Eng. 32 (1954) 35–53.
[60] T. Baldock, M. Tomkins, P. Nielsen, M. Hughes, Settling velocity of sediments at high concentrations, Coast. Eng. 51 (2004) 91–100.
[61] H. Nicolai, B. Herzhaft, E. Hinch, L. Oger, E. Guazelli, Particle velocity fluctuations and hydrodynamic of sedimenting non-Brownian spheres, Phys. Fluids 73 (1995) 12–23.
[62] B. Balakin, A. Hoffmann, P. Kosinski, L. Rhyne, Eulerian-Eulerian CFD models for the sedimentation of spherical particles in suspension with high particle concentrations, Eng. Appl. Comp. Fluid. 4 (2007) 116–126.
[63] C. Varsakelis, M. Papalexandris, The equilibrium limit of a constitutive model for two-phase granular mixtures and its numerical approximation, J. Comput. Phys. 229 (2010) 4183–4207.
[64] C. Varsakelis, M. Papalexandris, Existence of solutions to a continuum model for hydrostatics of fluid-saturated granular materials, Appl. Math. Let. 35 (2014) 77–81.
[65] E. Thompson, H. Huppert, Granular column collapses: further experimental results, J. Fluid Mech. 575 (2007) 177–186.
[66] L. Rondon, O. Pouliquen, P. Aussillous, Granular collapse in a fluid: role of the initial volume fraction, Phys. Fluids 23 (2011) 073301.
[67] C. Wang, Y. Wang, C. Peng, X. Meng, Dilatancy and compaction effects on the submerged granular column collapse, Phys. Fluids 29 (2017) 103307.